

# Hardware Tests for Proton Beam Therapy Calorimetry Research and Development Project Report

**Adam Knoetze**

Supervised by:

**Dr. S. Jolly**

**Prof. R. Saakyan**

**MSci Physics: PHASM201**

March 27, 2017

Department of Physics and Astronomy  
University College London  
Gower Street  
London  
WC1E 6BT  
United Kingdom



**Submission of coursework for Physics and Astronomy course PHASM201/PHAS3400**

Please sign, date and return this form with your coursework by the **specified deadline** to the Departmental Office.

**DECLARATION OF OWNERSHIP**

I confirm that I have read and understood the guidelines on plagiarism, that I understand the meaning of plagiarism and that I may be penalised for submitting work that has been plagiarised.

I confirm that all work will also be submitted electronically and that this can be checked using the JISC detection service, Turnitin®.

I understand that the work cannot be assessed unless both hard copy and electronic versions of the work are handed in.

I declare that all material presented in the accompanying work is entirely my own work except where explicitly and individually indicated and that all sources used in its preparation and all quotations are clearly cited.

Should this statement prove to be untrue, I recognise the right of the Board of Examiners to recommend what action should be taken in line with UCL's regulations.

Signed \_\_\_\_\_

Print Name \_\_\_\_\_

Dated \_\_\_\_\_

Title	Date Received	Examiner	Examiner's Signature	MARK

## Abstract

The capability of a CAEN DT5800D detector emulator was evaluated for reproducing experimental proton therapy calorimetry data collected at the Clatterbridge Cancer Centre. As part of the evaluation, the detector emulator was configured so that the aforementioned experimental data could be successfully emulated. The greatest limitation incurred when configuring for this emulation was the relatively coarse time-step between data points used to define the emulated signal shape. Despite this limitation, the detector emulator was evaluated to be suitable for testing hardware and software analysis tools in the absence of a detector or radiation source. However for future use, it is recommended that improved methods of constructing the required signal shape and energy spectrum are used. Furthermore, a means of converting data from a LeCroy binary waveform template to ASCII where information about the waveform can also be easily extracted was also developed. Finally, a preliminary investigation into how the addition of an active divider circuit in a photomultiplier tube (PMT) affects a PMT's response under different injected light pulse frequencies, in particular the gain-frequency response. It was observed that the active divider circuit did change the response and a frequency dependence was exhibited.

# Contents

<b>1</b>	<b>Introduction</b>	<b>5</b>
1.1	Overview of Radiotherapy Options . . . . .	5
1.2	Basic Ideas of Proton Therapy . . . . .	6
1.3	Limitations of Proton Therapy . . . . .	9
1.4	Current Quality Assurance Procedures for Proton Therapy . . . . .	9
1.5	Proposed Future Quality Assurance Procedures . . . . .	10
<b>2</b>	<b>Detector Description</b>	<b>12</b>
2.1	Scintillator Theory . . . . .	12
2.2	PMT Theory . . . . .	14
2.3	Detector . . . . .	17
<b>3</b>	<b>Experimental Results and Data Conversion</b>	<b>19</b>
<b>4</b>	<b>Detector Emulator</b>	<b>22</b>
4.1	Overview and Intended Use . . . . .	22
4.2	Abilities . . . . .	22
4.2.1	Energy Spectrum Emulation . . . . .	22
4.2.2	Signal Shape Emulation . . . . .	26
4.2.3	Time Distribution . . . . .	29
4.2.4	Emulator Output . . . . .	30
4.2.5	Noise and Interference Emulation . . . . .	31
4.3	Limitations . . . . .	33
4.4	Evaluation of Potential Uses . . . . .	34
<b>5</b>	<b>PMT Testing</b>	<b>34</b>
5.1	Rationale . . . . .	34
5.2	Experimental Set Up . . . . .	35
5.3	Method . . . . .	36
5.4	Results . . . . .	38
5.4.1	Wide Frequency Range . . . . .	38
5.4.2	Narrow Frequency Range . . . . .	41
5.4.3	Fixed Peak Current . . . . .	43
5.4.4	Anomalous Results . . . . .	44
<b>6</b>	<b>Conclusion</b>	<b>46</b>
	<b>References</b>	<b>47</b>

# 1 Introduction

## 1.1 Overview of Radiotherapy Options

Currently, the three most common methods of treatment a cancer patient can undergo are surgery, chemotherapy and radiotherapy. Each of these treatments have associated advantages and disadvantages, which are considered when choosing the most suitable course of treatment the specific patient. Besides the stage of tumour, two of the most important factors taken into consideration when choosing a course are the size and location of the cancerous cells/tumour.

Surgery, if feasible, is an effective treatment as it involves the physical removal of the tumour. However, due to its invasive nature, if the tumour is located in a hard to reach location or is in close proximity to sensitive/easily tissue, the complexity of the procedure will increase. Often the potential surgical procedure is so complex the it would be ill-advised to proceed and another method of treatment is considered. Furthermore, if the cancer is spread over a large region, a single or multiple surgical procedures may not be able to remove all of the cancerous material and a non localised procedure like chemotherapy may be more suitable.

Chemotherapy is a well practised method of cancer treatment that can better treat scenarios where surgery falls short, however the way this is achieved introduces different side-effects. This treatment consists of giving the patient a dose of cytotoxic drugs that target cancerous cells [1]. Although this brings the benefit of the procedure being non-intrusive, it means that the treatment is non localised and therefore brings about unwanted side-effects, including damaging healthy cells. These are effects can be minimised by controlling the dosage over time but cannot be avoided.

Another form of non-invasive radiotherapy, which is most comparable to proton therapy, is photon/X-Ray radiotherapy. This consists of typically using a linear accelerator to accelerate electrons into a metal plate which via bremsstrahlung radiation generates a beam of high energy photons, usually in the X-Ray region of the electromagnetic spectrum. This beam is used to deliver a dose of ionising radiation to the patient which damages the DNA inside the cancerous cells. The major unwanted side effect that occurs with this procedure is that the photons do not only irradiate the cancerous cells but all cells along their path, causing unwanted additional damage. Furthermore, in order to deliver a high enough dose at the tumour, higher energy photons need to be used to compensate for the loss of energy via attenuation (and other methods) between the source and tumour. This therefore means that a higher dose is received in the cells before the tumour.

With this treatment methods, photons are not stopped by the tumour and therefore continue on their path and continue to deliver a smaller dose to cells beyond the tumour. Due to the limitation

of dose containment, X-Ray radiotherapy is also limited by tumour location due to the potential sensitivity of neighbouring tissue. This limitation is extended by the irreversible damage that may be caused in young patients who are more susceptible to side-effects during early development. An alternative treatment that has the advantage of delivering significantly less of the overall dosage outside of the intended treatment area is proton therapy.

## 1.2 Basic Ideas of Proton Therapy

The use of protons as a form of radiotherapy was first proposed by R. Wilson in 1946 [2], with the first patients being treated at the Lawrence Berkeley Laboratory in 1954 [3] with the first hospital based treatments capable of targeting deep tumours becoming available in 1990 at Loma Linda University. Currently in the UK there is only one NHS centre for proton therapy, located at the Clatterbridge Cancer Centre in Wirral, Merseyside. This centre consists of a 62 MeV cyclotron that provides a proton beam, which is then reduced in the beamline to 60 MeV. The proton beam facilities at the centre are used to treat tumours in the eye of up to 31 mm in depth. Two new centres in the UK are currently under development, including a centre at University College Hospital due for completion in 2018.

Proton therapy holds the same key principles as X-Ray radiotherapy whereby particles, now protons, are accelerated using either a linear accelerator, cyclotron or synchrotron to high energies to deliver a dose to a tumour. In the beamline, upstream from the patient, after the accelerator a series of collimator, stoppers and other devices to shape the flux of the beam front for the application [4]. For example, this may be to 'flatten' the Gaussian distribution of the flux to an even distribution so that a cell hit by the edge of the beam receives the same dose as one hit directly by the central part of the beam to improve the method of which the target tumour is treated.

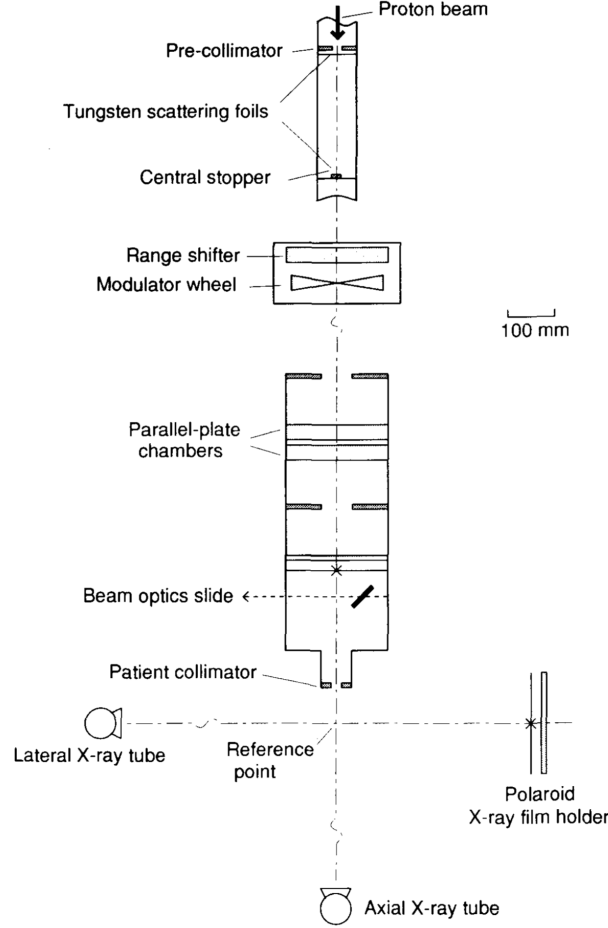


**Figure 1:** [4] Sketch of the arrangement of the proton beamline at the Clatterbridge Cancer Centre. Note the inclusion of the stopper and collimators to modify the beam front, and modulator wheel to modify the shape of the total Bragg Peak.

The advantage of proton therapy in minimising the dose delivered outside the intended treatment area is achieved through the exploitation of the Bragg peak associated with the dose distribution of a proton in a medium. Protons have mass therefore they lose energy as they traverse through a medium, this can be modelled using the Bethe-Bloch formula, which gives rise to a Bragg peak. The Bethe-Bloch formula describes the mean rate of energy loss by relativistic heavy particles when travelling through matter [5] (see eq.(1)). Where  $E$  is energy,  $x$  is the mass per unit area,  $K$  is a constant represented by eq.(2),  $z$  is the charge of the incident particle,  $Z$  is the atomic number of the absorber,  $A$  is the atomic mass of the absorber,  $c$  is the speed of light in free space,  $\beta$  is the ratio of the particle's velocity to  $c$ ,  $m_e$  is electron mass,  $\gamma$  is the Lorentz factor,  $W_{max}$  is the maximum energy transfer in a single collision (see eq.(3)),  $I$  is the mean excitation energy,  $\delta(\beta\gamma)$  is the density effect correction to ionisation energy loss,  $N_A$  is Avogadro's number and  $r_e$  is the classical electron radius. This formula gives rise to the Bragg peak when applied for a proton.

$$-\left\langle \frac{dE}{dx} \right\rangle = Kz^2 \frac{Z}{A} \frac{1}{\beta^2} \left[ \frac{1}{2} \ln \frac{2m_e c^2 \beta^2 \gamma^2 W_{max}}{I^2} - \beta^2 - \frac{\delta(\beta\gamma)}{2} \right] \quad (1)$$

$$K = 4\pi N_A r_e^2 m_e c^2 = 0.307\,075 \text{ MeV mol}^{-1} \text{ cm}^2 \quad (2)$$

$$W_{\max} = \frac{2m_e c^2 \beta^2 \gamma^2}{1 + 2\gamma m_e/M + (m_e/M)^2} \quad (3)$$

By adjusting the energy of the dose delivering protons, the Bragg peak at the end of the proton path can be positioned over the target area. If calibrated correctly, less of the dosage is deposited in healthy tissue before the target area than with X-Ray radiotherapy and considerably less afterwards due to a sharp fall in dose beyond the Bragg peak [6]. The beam can be further modified so that the Bragg peak is widened to create a plateau of similar dosage delivered near the end of the proton path through the utilisation of protons varying energies, typically referred to as a spread-out Bragg peak (SOBP) (see Fig.2). This is a useful beam characteristic as it allows a larger volume of the target tumour to be treated at once which can be achieved by using a rotating range modulator wheel [7].

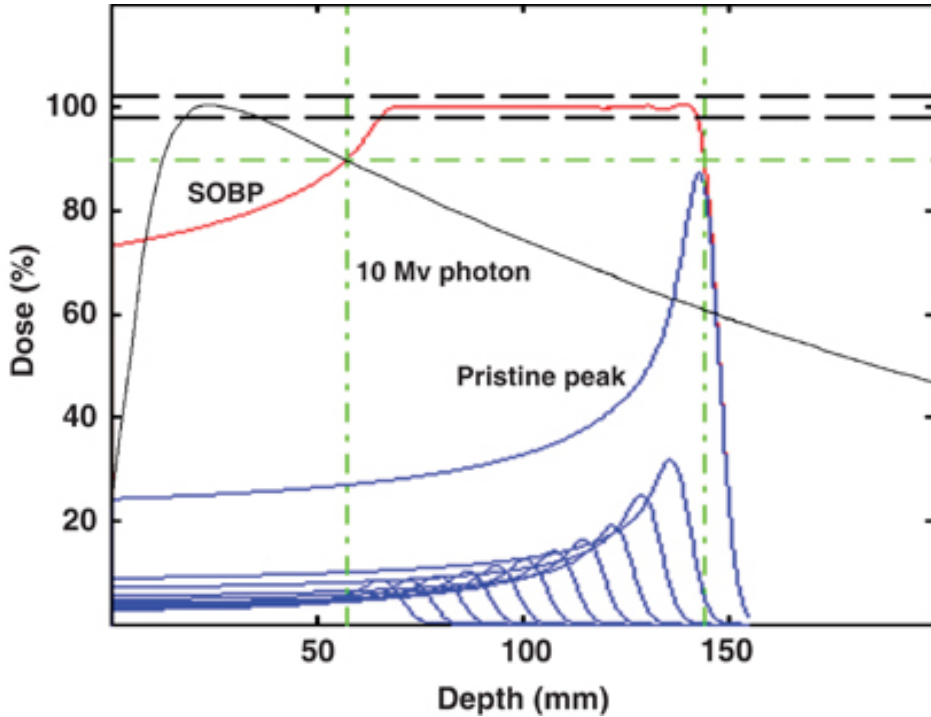


**Figure 2:** [8] Plot showing the depth-dose distributions for a 10 MV photon beam (black), SOBP proton beam (red) and single protons (blue, labelled pristine peak). Each “pristine peak” shows the Bragg peak of the individual constituent protons of different energies that make up the SOBP. The green dot-dashed lines indicates a region over which 90% of the dose and . Note the peak in dose of the photon curve at  $\sim 20$  mm before the 90% dose region and the continuation of the dose beyond the latter 90% line compared to the largest pristine peak where the dose before the 90% dose region is substantially less than its peak dose and the absence of dose beyond the peak.

The above described features of proton therapy make it a suitable candidate for the treatment of difficult to reach tumours such as ocular (uveal) melanoma and sarcomas in the spine where the surrounding tissue and nerves would otherwise potential be irreversibly damaged. The improved



localisation of the dose to the treatment region also makes this course of treatment a more favourable option in young children.

### **1.3 Limitations of Proton Therapy**

The major limitation of proton therapy arises from its key advantage, whereby the localisation of the treated area through the exploitation of the proton Bragg peak means that the effectiveness of the treatment ultimately relies on the confidence of the positioning of the Bragg peak. If this limitation is not considered before a course of treatment the Bragg peak may be positioned such that the majority of the dose may fall on healthy tissue rather than the intended treatment area and cause more harm to the patient. This is of increased importance as not each patient is alike and individual patients often lose mass over a course of treatment meaning that adjustments do not only need to be made on a patient by patient basis but for every round of therapy.

The potential risks associated with this limitation are minimised through in depth analysis of the beams characteristics through simulations, testing, and via routine calibrations/checks. These routine calibrations and checks are repeated daily, weekly, monthly, or less frequently depending on their contribution to the overall effectiveness of the treatments, and are usually referred to as quality assurance procedures. The most important of which, and what focus of this project relates to, is the performance of dosimetry on the proton beam which provides information on the proton beam dose output, range, Bragg peak width. These daily quality assurance procedures are critical for optimum performance and patient safety.

Further limitations and challenges associated with proton therapy include the cost of constructing dedicated treatment centres, the cost and time required to train current or new hospital staff on the technologies and techniques associated with proton therapy, and without trial tumours in some positions may be better treated with photon based radiotherapy.

### **1.4 Current Quality Assurance Procedures for Proton Therapy**

Quality assurance procedures include measurements of the proton beam dose output, range, Bragg peak width and machine safety checks. Current methods of measuring the beam range include measuring the depth of certain dose levels in water [9], water-like plastics (water phantom) or radiographic film [10][11].

Water tank dosimetry, as previously stated, is the process of measuring the depth, inside a water tank, at which the beam delivers a certain percentage of the dose. This information is used to find the position and width of the Bragg peak. This is a very time consuming process, and if performed

daily occupies time that could potentially be spent using the machinery to treat patients. Clinically, for convenience, a water phantom with a silicon diode is used rather than an actual water tank [12]. A water phantom is a, typically, solid block of material with similar radiation characteristics to water.

Radiographic film is a faster alternative to water tank dosimetry and can be used in both photon and proton therapy dosimetry. When a proton beam falls incident on and irradiates radiographic film, it will cause the film to change colour. Analysis of the optical density of the now coloured irradiated film can be used to determine the dose received. However radiographic film can under-respond at the Bragg peak and is not well suited to low dosages. This method can also be used to obtain the lateral beam profile as differences in the optical density across the region where the beam fell incident on the film can be measured [10].

Clinically a multilayer ionisation chamber, such as an IBA Zebra [13][14], is typically used to take depth-dose measurements. This is a commercially available device that is used at many proton therapy clinics in quality assurance procedures in North America and Europe. The IBA Zebra device consists of 180 parallel plate ionisation chambers separated by a high density, water equivalent material. Each ionisation chamber provides a measurement of the dosage at the respective depth, which when combined provides a full depth-dose profile for the proton (or photon) beam inside the device. Hence, in the proton beam case, this allows the operator to observe the Bragg peak in a relatively quick and simple manner. As this is a commercial device, little information about it has been made public, few papers have been published about its performance and it is required that propriety software is used to acquire data. Despite this, investigations have reported that the IBA Zebra can efficiently produce repeatable dose depth measurements that do not suffer a significant loss in accuracy for the time required to take the measurement when compared to other well established ionisation chamber/water phantom methods [15].

Additional beam information is typically measured daily [16], such as beam flux using a Faraday cup [17]. However this measurement cannot be used to determine the shape of the Bragg peak. A Faraday cup blocks the entire beam and is used to determine the exact number of protons leaving the nozzle [18]. This is achieved by measuring the total collected charge of the protons that fall incident on the cup [19][20] and is calculated simply by dividing the total charge collected by the Faraday cup by the elementary charge,  $e$ .

## 1.5 Proposed Future Quality Assurance Procedures

It is proposed to develop a new method of quality assurance that is faster than and as precise as water tank dosimetry in finding the proton energy and determine the range. This method

involves the use of water-like plastic scintillator and photomultiplier tube (PMT) to determine the beam characteristics (Pairing of a plastic scintillator block with a PMT is often referred to as an optical module). The end goal being the construction of a device of this nature that can be attached to the end of the beam nozzle that will shorten the time spent completing routine quality assurance procedures. It is predicted that this method will simplify the quality assurance procedure and enable more patients to be treated per day, even more so than with the use of the IBA Zebra device. Investigations into the use of plastic scintillation detectors for radiotherapy have been carried out before, and have been shown to measure the depth-dose profiles for x-ray and electron beams with a better spatial resolution than ionisation chambers, radiographic film and silicon diodes [21]. This has also been shown to be the case with a proton beam at a rate faster than the previously mentioned methods [22].

The detector being developed will be largely based upon the optical module design research and development completed for the calorimeter in the SuperNEMO double beta decay experiment (see Fig.3), a modified version of a SuperNEMO optical module has been shown to give encouraging results in this application. The new detector will not have to be as large as a SuperNEMO optical module as the scintillator only needs to cover a narrow beam of protons, but will share many similar characteristics including having the same wrapping. The wrapping consists of a layer of PTFE (Teflon) and aluminised Mylar [23] to provide a desired level of reflectance inside the block and prevent light leakage. Another investigation [24] into the use of scintillation detectors for proton radiotherapy showed that it was competitive and far cheaper than conventional systems for measuring the beam range.

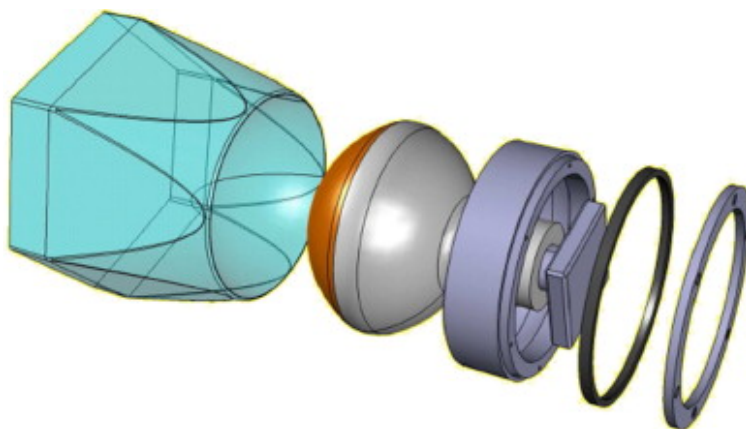


**Figure 3:** Drawing of a proposed optical module for the SuperNEMO experiment. Note the clear tinted scintillator (blue, colour from doping) and round PMT with brown translucent photocathode. [25]

## 2 Detector Description

### 2.1 Scintillator Theory

Scintillators are widely used in the detection of ionising radiation. Scintillating materials produce short “flashes” of light through fluorescence or phosphorescence in response to interactions between the material and external particles. When coupled, for example, with a PMT or photodiode, the pair can be used in radiation spectroscopy.

Scintillators can be grouped into two main categories based upon their chemical composition; organic and inorganic scintillators [26]. Organic scintillators can then be sub categorised into: pure organic crystals, liquid organic solutions, plastic scintillators, thin film scintillators and loaded organic scintillators. With the most commonly used being liquid and plastic. There also many categories of inorganic scintillators, with the most common being alkali halide crystals such as NaI(Tl). When comparing the two categories, generally organic scintillators have a faster response time, and inorganic scintillators have a greater light yield and linearity. As the scintillator used in the prototype detector was plastic, only this subcategory and its encompassing category will be discussed further in this report.

Organic plastic scintillators have a high density and have a composition consisting of a solvent/base plastic, the primary fluorescent/scintillating material and a fluor/dopant. Two common materials for this type are doped polyvinyl-toluene (PVT) and polystyrene. The scintillation mechanism in organic scintillators arises from energy level transitions in the molecules of scintillator. When a particle enters the scintillator, it loses kinetic energy which is deposited in the material. The additional energy excites the molecules of the primary fluorescent moving electrons in the molecule into a higher energy level. These then de-excite emitting photons, these are then reabsorbed by the secondary fluorescent (fluor) who’s molecules are then in turn excited. The secondary fluorescent (fluor) then de-excites, acting as wavelength shifter, emitting photons typically in blue/UV range of the electromagnetic spectrum. If a scintillator exhibits this response and produces light of a longer wavelength than what is absorbed it is described as phosphorescent.

Important scintillator characteristics and responses that need to be taken into account include: linearity of the light yield response from charge particles, the time response/decay time of the scintillator, the light pulse shape from different particles, radiation damage [33] and potential Cherenkov radiation [27].

A semi-empirical formula (see eq.(4)) that accounts for quenching effects known as Birks’ Law can be used to model non-linearity of light yield from organic scintillators [28]. This formula provides

a relation between the light yield per unit length,  $\frac{dL}{dx}$ , to the energy emitted per unit length,  $\frac{dE}{dx}$ . Where  $k_B$  is a user determined parameter, used to fit experimental data, known as Birks' constant and  $S$  is the scintillation efficiency. Quenching is a collective term used to acknowledge the existence of some radiationless de-excitation from damaged molecules [29]. It is important that the light yield behaviour of a scintillator being used in proton therapy quality assurance is known as any information incorrectly interpreted carries a safety risk for patients.

$$\frac{dL}{dx} = \frac{S \frac{dE}{dx}}{1 + k_B \frac{dE}{dx}} \quad (4)$$

The fluorescence intensity of plastic scintillator is time dependent and for many applications this can be modelled using exponential decays. The time response depends on the time it takes to populate higher energy levels and the fluorescence/phosphorescence decay time. This can be modelled using eq.(5) where  $I$  is the intensity,  $\tau_1$  is the population time constant and  $\tau$  is the fluorescence decay constant. Using eq.(5), light pulse curves can be generated which differ depending on the source of radiation and particle make up of the radiation (see Fig.4). Hence it is possible to use experimentally acquired light pulses to discriminate between sources of radiation [30]. Furthermore a time delay can also occur in physically larger scintillator blocks, arising from the time it takes a photon to traverse the distance between the emission site and attached detector. This time is often negligible.

$$I = I_0 \left( e^{-t/\tau} - e^{-t/\tau_1} \right) \quad (5)$$

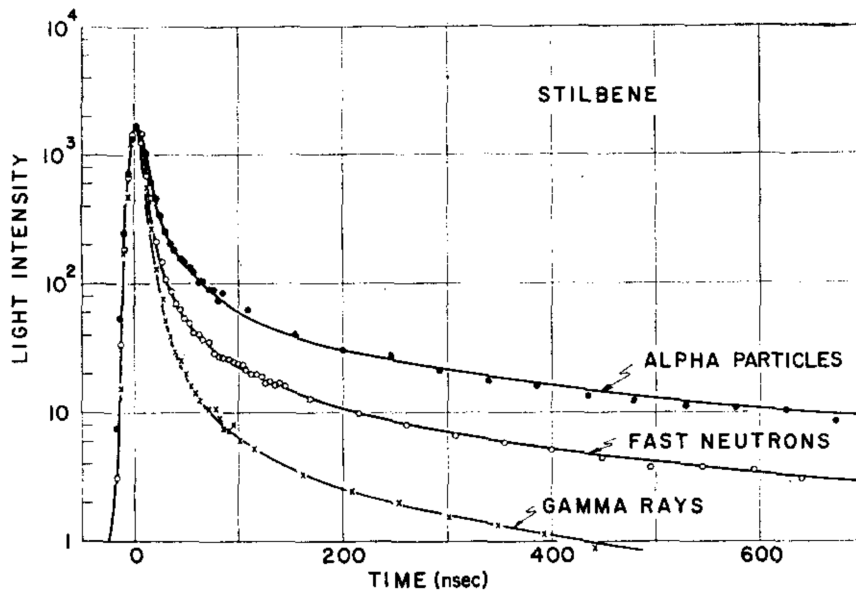


**Figure 4:** Scintillator light pulse acquired in stilbene for alpha particles, fast neutrons and gamma rays. Note the distinctly different tails shapes for each of the radiation types. [31]

Radiation damage can occur in plastic scintillators after prolonged exposure to ionising radiation. This can lead to a lower light yield from and tends to arise from optical changes in the base plastic/solvent rather than chemical changes in the fluors [32][33]. If scintillator/PMT based quality assurance methods are adopted for proton therapy, this should be taken into account over the detector's lifetime.

Cherokov radiation may occur within the scintillator block, any optical fibers attached to the scintillator, or if one is used, a light guide. If produced, the Cherenkov light may be picked up by an attached PMT or photodiode [34].

## 2.2 PMT Theory

Secondary emission, which underpins the amplification process for a PMT, was first reported by I. Austin and H. Starke in 1902 [35]. A new method for amplifying weak photocurrents by using a source cathodes and a series of dynodes supplied with increasing potential difference between them (amplification via secondary emission) was first developed by L. Kubetsky in 1930 [36]. This device would later become known as a photomultiplier tube (PMT). Although this is often credited to V. Zworykin, who was involved in early PMT development. Since it's initial conception, PMT usage has been widespread throughout many areas of academic research, especially in the field of high energy physics.

The key components of a PMT are; the photocathode, dynodes, the collector anode and the vacuum enclosure (see Fig.5). The photocathode takes the form of a thin, nano-scale layer that lines the entrance/window of the PMT, when a photon strikes the photocathode it is adsorbed and photoelectrons are emitted, via the photoelectric effect. Due the nature of the photoelectric effect, the incoming photon needs to be of a high enough energy so that the emitted photoelectron can overcome the work function and escape from the photocathode's surface. The emitted photoelectron is then accelerated towards the first in a series of dynodes (electrodes). Upon striking the first dynode, the photoelectron deposits its energy into the dynode and (usually) between 1 and 5 photoelectrons are re-emitted from the dynode's surface. These new photoelectrons are then accelerated towards the next dynode and the secondary emission process is repeated resulting in a multiplicative effect in the number of electrons. Once all the dynodes have been circumnavigated, the now many photoelectrons are collected on the anode and a signal can be readout from the PMT. This process roughly produces order  $\sim 10^6$  photoelectrons from a relatively weak light pulse from a scintillator block. A signal of this size is more easily analysed. The above listed, constituent components of a PMT need to be contained inside a vacuum enclosure in order for it to exhibit this amplification.

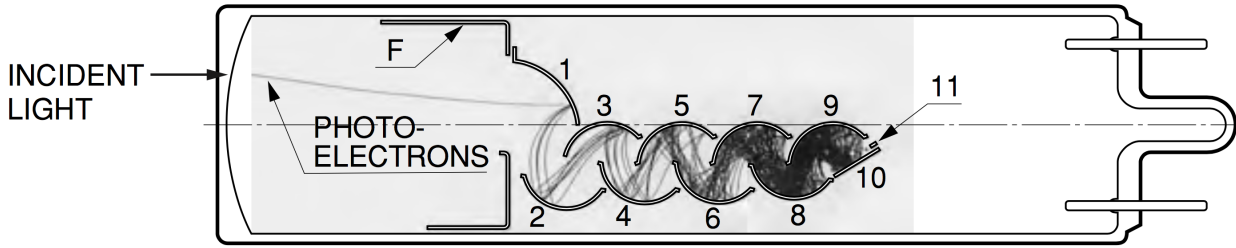


**Figure 5:** Internal structure of a Linear-Focused type PMT. Components labelled 1 - 10 are dynodes, 11 is the anode, F is the focusing electrode and the photocathode would be located on the far left of the tube. The electron trajectories between dynodes have been included, these highlight the electron multiplication effect. This PMT structural type offers very fast response times and large output currents. It is therefore suitable for applications where good a time resolution and pulse linearity is require. [37]

A useful parameter often assigned to PMTs by manufacturers that can be used to quantify the detectors response characteristics is quantum efficiency,  $\eta$ . This assigns a percentage value for the sensitivity of the photocathode based upon the average number of photoelectrons emitted per incident photon (see eq.(6)) [38]. Hence, a “perfect” photocathode would have  $\eta = 100\%$ , however most photocathodes have a peak quantum efficiency of  $\eta \simeq 30\%$ . Quantum efficiency can also be represented as a function of wavelength,  $\lambda$ , where  $S$  is radiant sensitivity of the photocathode (see eq.(7)). Depending on the intended application, the quantum efficiency at peak wavelength needs to be considered when choosing a PMT.

$$\eta = \frac{\# \text{ emitted photoelectrons}}{\# \text{ incident photons}} \cdot 100 \quad (6)$$

$$\eta = \frac{hc}{\lambda e} \cdot S \cdot 100 \approx \frac{1240}{\lambda} \cdot S \cdot 100 \quad (7)$$

A simple estimation of the gain,  $g$ , of a PMT can be calculated via a function (see eq.(8)) of the number of dynodes,  $N$ , and the average dynode secondary emission ratio,  $\delta$  [39]. As already stated, a typical dynode emits between 1 and 5 electrons per incident electron and  $\delta$  is not constant. Therefore the approximation of  $\delta = 3$  is often used. The statistical nature of this secondary emission process and the initial photoemission from the photocathode imply an ever present statistical noise to the PMT signal.

$$g = \delta^N \quad (8)$$

The output (voltage) signal from a PMT can be modelled using either a double or single exponential equation (eq.(9)), depending on the resistance,  $R$ , and the capacitance,  $C$ , of the anode (and other elements in the output circuit). If the time constant of the scintillator,  $\tau_S$ , equals the time constant of the output circuit,  $\tau = RC$ , then the single exponential should be used. The double

exponential for should be used for all other values of  $\tau$ . In eq.(9),  $N_{p.e.}$  represents the number of photoelectrons emitted at the cathode [38].

$$V(t) = \begin{cases} -\frac{gN_{p.e.}eR}{\tau-\tau_s} \left[ e^{-\frac{t}{\tau_s}} - e^{-\frac{t}{\tau}} \right] & \text{if } \tau \neq \tau_s \\ \left( \frac{gN_{p.e.}eR}{\tau_s^2} \right) t e^{-\frac{t}{\tau_s}} & \text{if } \tau = \tau_s \end{cases} \quad (9)$$

Many choices of PMT with different internal dynode structures are commercially available. The choice in structure should be based upon the application and physical limitations. This is because different structures provide varying response times, pulse linearities, electron collection efficiencies etc. For example, a circular focussed grid PMT that is mounted side on to the radiation source has the dynodes arranged in a way that minimises the time of flight for electrons by optimising their trajectories between dynodes. For the purpose of proton therapy quality assurance where the detector is nozzle mountable, a head-on PMT is more suitable.

Voltage dividers, chains of resistors and capacitors, are used in PMTs to regulate the voltage between dynodes. Voltage dividers therefore aid in minimising variation in gain and linearity.

When there is no incident light on the photocathode a PMT will still exhibit an anode current. This is referred to as the PMT's dark current. This typically originates from thermionic emission current from the dynodes and cathode [40], leakage currents from electrode support materials, radioactive contaminations, ionisation from residual gases in vacuum enclosure and light from electrode glow. Dark current is not constant and has random variations and not only does it provide a small background signal, its randomness contributes to signal noise. It is therefore desirable to have minimal dark current.

External environmental conditions can also effect the response of a PMT. This includes ambient light exposure, external magnetic fields and to a lesser extent temperature. If while under voltage and PMT is exposed to ambient light there is a high risk that the PMT will be damaged or destroyed. It is therefore critical that while under operation a PMT is kept in complete darkness, or as close to complete darkness as possible. External magnetic fields may interfere with the electron trajectories between dynodes, which in turn may reduce the overall PMT efficiency. In cases where the PMT will be subject to significant external magnetic fields, mu-metal magnetic shielding can be used, or in less extreme cases the PMT can be simply aligned to respectively to the magnetic field to mitigate its effect. Temperature changes may lead to changes in the photocathode band structure. An increase in temperature generally leads to an increase in dark current and a change in PMT gain [38].



## 2.3 Detector

The prototype detector existing at the time of this project consisted of a Polystyrene scintillator coupled via Saint Gobain BC-630 silicone optical grease to a 2-inch photomultiplier tube all encased within light-tight housing. At the time of this report, there existed two versions of the prototype detector. Both versions utilised the same scintillator block however used different, identical PMTs with different electronics bases. The version used to take experimental data had an electronics base manufactured by Hamamatsu, this base included an “Active Divider Circuit”, the details of which have been kept confidential by Hamamatsu. The second version of the detector, used for comparisons, utilised an in-house manufactured electronics base identical to the Hamamatsu base but without the inclusion of an “Active Divider Base”. From here onwards, the two versions will be referred to as “Hamamatsu base” and “UCL base”.

The Polystyrene scintillator block was cuboid and measured 3 cm by 3 cm by 5 cm. This was wrapped in 12  $\mu\text{m}$  of PTFE around the sides and 76  $\mu\text{m}$  of metallised Mylar around the sides of the block and face not in contact with the PMT. The wrapping is to improve the reflectivity inside the block so that the probability of the photons from scintillation reaching the PMT photocathode.

The PMT in the prototype detector is a 2-inch (52 mm) Hamamatsu R13089 head-on linear focussed tube with 8 dynode stages and a 46 mm diameter Bialkali photocathode (see Fig.6). A typical voltage-gain response plot, provided by Hamamatsu, for this model PMT can be seen in Fig.7. The compact nature of this scintillator and PMT allows for improved timing when compared to larger similar detectors, and provides a significant step forward in the development of a detector smaller enough be mounted on a proton therapy beamline nozzle.

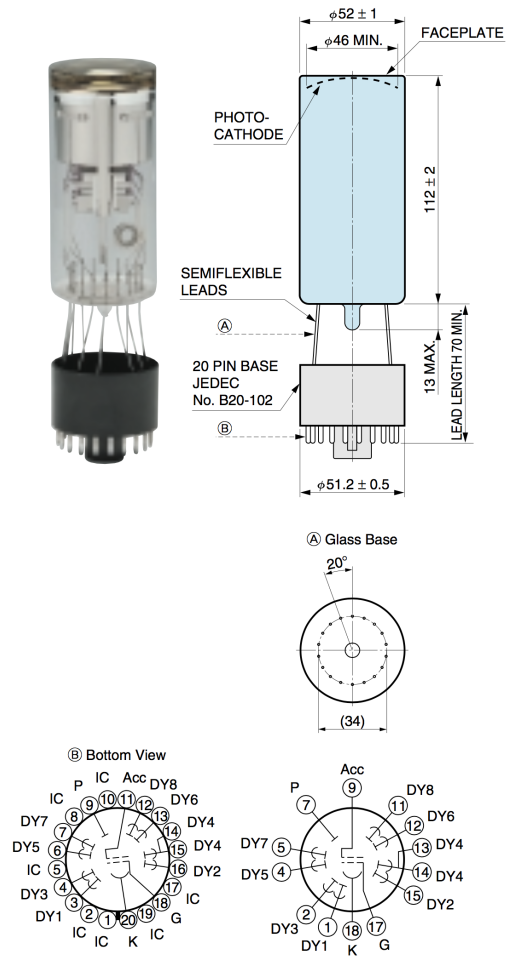


**Figure 6:** Image and dimensional outline of a Hamamatsu R13089 photomultiplier. Schematic also indicates the dynode positions within the PMT. [41]

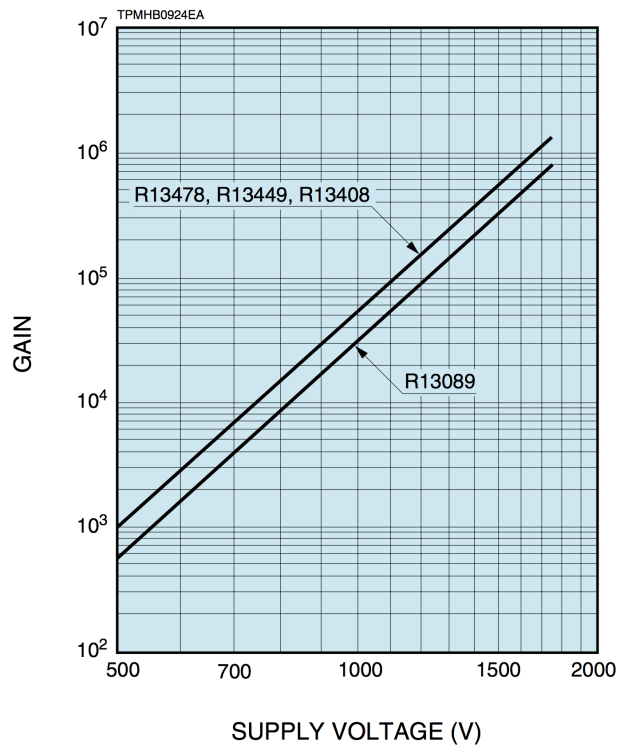


**Figure 7:** Gain response of a Hamamatsu R13089 photomultiplier across its range of supply voltages, supplied by manufacturer. [42]

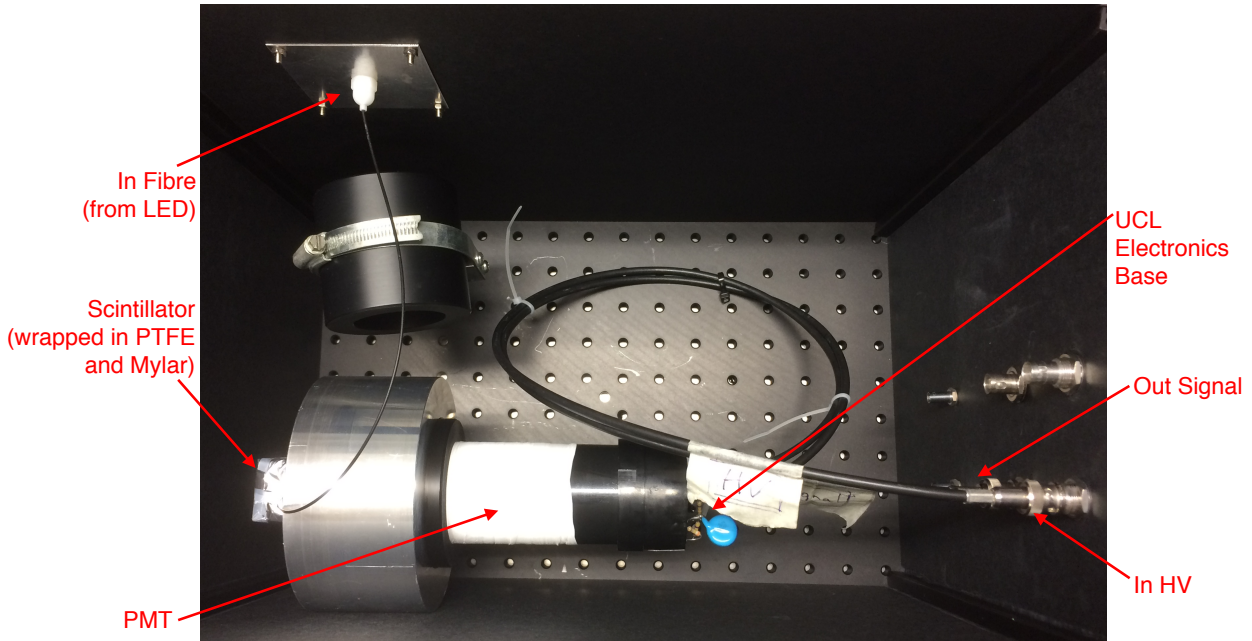


**Figure 8:** Photograph of the prototype detector with the UCL base PMT inside the light-tight housing. In the photograph, the fibre for pulsed light injection is attached to scintillator

### 3 Experimental Results and Data Conversion

The first task completed was developing a familiarity with a Teledyne LeCroy HDO6104 oscilloscope [43]. This device was and will be continued to be used to record data from detector tests, including data collected using the proton beam at the Clatterbridge Cancer Centre.

The first function required to be investigated and then configured was how to record data at a fast enough rate which could be recorded in a continuous manner. After various simple tests recording data using the inbuilt methods on the oscilloscope produced at different rates by a primitive signal generator, it was observed that the limiting factor when recording data was the oscilloscope's hard drive disk (HDD) write speed. It was observed that there were gaps in the recorded data when data files were being written to the HDD. Therefore, it was decided that data would be recorded in binary format rather than in ASCII. The binary format generated data files significantly smaller in size, reducing the time required to write the files to the HDD and hence reducing the time elapsed between data files.

Furthermore, the sequence sampling mode was chosen to record the data, this mode writes a defined number of waveforms from triggering events to a buffer, hence giving the ability to record and write multiple waveforms at once in a single compound waveform. This method is superior to writing individual waveform files because it requires fewer files to be written, allowing sequential waveforms to be observed which may otherwise be missed due to files being written. One negative

feature of the sequence sampling mode is that it cannot be used to determine the trigger rate because when triggered, this mode simply appends the current waveform to the end of the previous waveform (see Fig.9). Therefore not recording any data in-between triggered events and eliminating the possibility of deducing the trigger (or signal) rate from the recorded data.

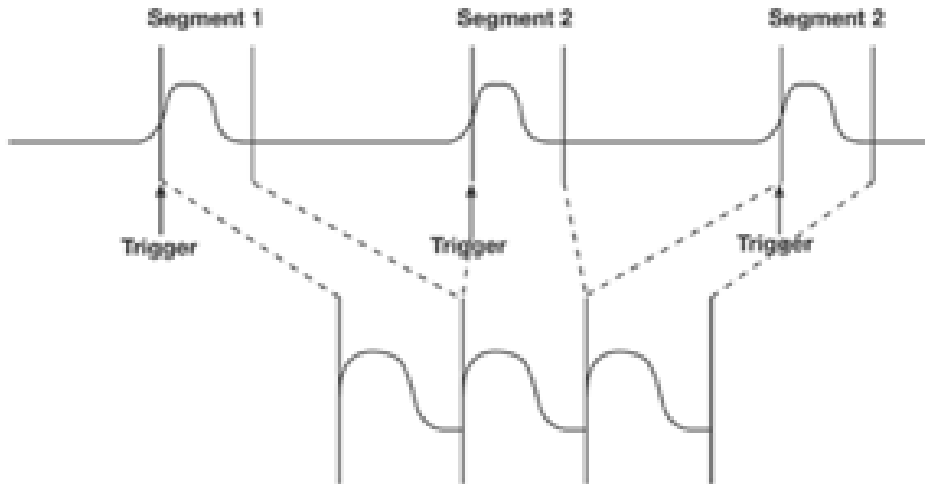


**Figure 9:** Diagram illustrating how individual waveforms are concatenated using the sample sequencing mode on a Teledyne LeCroy HDO6104 oscilloscope. Top section shows continuous input signal. Bottom section shows the form of the produced aggregate waveform.

As previously stated, data collected using the HDO6104 oscilloscope was recorded in binary. Binary data is written to a .trc file formatted in accordance with the LeCroy\_2\_3 Waveform Template [44]. Data in this format therefore had to be converted to ASCII and formatted suitably for compatibility with pre-existing data analysis programs. This was achieved by modifying a Python script [45] similar to a Matlab script provided by LeCroy. The choice was made to use Python due to no prior experience with Matlab. The Python script that was modified formed a good starting point as it could already convert single data file to ASCII. However the version existing at the time of the first modifications was poorly formatted, slow and did not perform the tasks that were required.

The modified script produced, had to have the ability to deal with the header which is generated at the top of every binary waveform data file. The header contains some useful information regarding the saved waveform, some of which is not typically recorded when writing to an ASCII file. However most of the information in the header is not useful for the intended use of the oscilloscope and therefore only increases the dead time between the data in recorded data files. Unfortunately the creation of this header appears unavoidable and due to the nature of the waveform template the retrieval of information for the header was not trivial. Some of the information was accessible in the original Matlab and Python scripts, but following modifications all but two items in the header were made accessible. In doing this, the produced script was made more object-orientated.

This task was not without its difficulties. The first incurred was the file size of the converted data files. It was expected that the file sizes would be much larger, however due to floating point values being automatically formatted into standard form with trailing decimals, they were larger than expected,  $\sim 400$  MB for a 1000 waveform data file. After further modifying the Python script, this was reduced to  $\sim 60$  MB.

Another issue arose from changing the ASCII data time column to the required format. This was not as straight forward to solve and required more investigation. It was initially requested that the time column start at zero and be continuous. However this was not appropriate as the sample sequence mode was used to record data. The time column was therefore reformatted to start from 0.0 ns and increase in 0.4 ns steps over 2502 lines and repeat. Setting each waveform duration to 1000.4 ns.

The 0.4 ns step size was found by inspection of converted data files (conversion script now finds this automatically). The length of 2502 lines per waveform was identified by writing a simple Python program which used factors of the total number of lines in a single data file to split the data. Once split, the voltage readings for each waveform were summed and binned into a histogram. The histograms produced were compared and the histogram generated from 2502 line length waveforms was the shortest that only produced a single peak similar to that of an ADC spectrum (see Fig.12). This was checked using data from different frequency runs and was still found to be the most suitable length. However at very high frequencies additional peaks start to appear and enlarge. This is expected if the waveform time duration is kept the same when recording data. An additional check by plotting an entire data file identified that the peaks were evenly spaced 1000.4 ns apart.

The modified conversion Python script initially took a long time to run, therefore the decision was made to attempt to rewrite it in Java, using the original Matlab script and waveform template as a guide. Unfortunately, this proved difficult to do and progress time consuming. Eventually focus was redirected to optimising the existing Python script so that it ran faster. The attempt to rewrite this in Java was not continued, this however should not be viewed as a failure, as now it is now known how the Python and Matlab programs work through studying the waveform template. Through further optimisations and modifications to the Python script, the conversion time per 51 file data set was cut down from an initial  $\sim 5$  hours to  $\sim 20$  minutes (on a personal laptop).

## 4 Detector Emulator

### 4.1 Overview and Intended Use

A CAEN DT5800D Desktop Digital Emulator was purchased with the intent of eventually using its capabilities to stress test the prototype detector, test other pieces of hardware, and analysis software. In order to reach this stage, relevant emulator functions needed to be tested and their usefulness evaluated.

The DT5800 series is, according to the manufacturer, the worlds first single device for the emulation of random signals from radiation detectors. Therefore allowing tests to be conducted in the absence of a radiation source and/or detector. The DT5800D model is the dual channel desktop version from the series (single channel, NIM compatible, touch screen, “micro” form-factor and faster rise time models have also been produced). This model allows the emulation of two separate radiation sources simultaneously. In summary, the detector emulator combines the features of a pulser, tail generator, waveform generator, waveform recorder and pulse generator in one device with a single software interface

The documentation provided with the detector emulator gave a brief but detailed description of the hardware and firmware architectures. This includes an overview on how signal shapes and artificial noise is generated. Unfortunately, the documentation lacks a satisfactory description on how to implement the devices features via the software interface. Therefore, in order to evaluate the potential of the detector emulator and to even just to learn how to use the device, it was necessary to test each of the features relevant to the initial intended use.

### 4.2 Abilities

All of the following tests performed to evaluate the performance of, and learn how to use the detector emulator were completed using experimental data collected at the Clatterbridge Cancer Centre (02/08/16) using the previously mentioned Teledyne LeCroy HDO6104 oscilloscope. To test and evaluate the key features of the detector emulator, the aim to emulate experiential data from the previously mentioned data set. The details of the features and methods as to configure the device to meet this aim as follows:

#### 4.2.1 Energy Spectrum Emulation

The DT5800D detector emulator has the ability to generate signal pulses with either a fixed amplitude/energy, with amplitudes that follow a predefined sequence of energies, or with amplitudes in accordance with an energy spectrum.

For the fixed amplitude/energy mode, the amplitude is set via the software interface and can take values between 0 V and 2.2 V (can be set in volts, LSB or if calibrated in keV). In fixed energy mode the emulator behaves similarly to a simple pulser.

When using the sequence mode, the predefined sequence of energy values must be imported as .csv file and formatted as specified in the detector emulator user manual. This mode is particularly suitable for experimental data that needs to be emulated exactly how it was recorded (i.e. not pseudo-randomly).

Before using the energy spectrum mode to specify the signal pulse amplitude distribution, the spectrum needed to be defined. The spectrum can either be defined using the inbuilt spectrum editor tool, where the user can choose to draw a spectrum from scratch or load a predefined spectrum from a database of spectra for isotopes, or defined by importing a correctly formatted .csv or CAEN digitiser .dat, spectrum .spectrum or ANS4242 .xml file. Once imported, the spectrum can be transformed/modified via the software interface. The emulator then uses the defined spectrum and a pseudo-random number generator to generate pulses with different energies with a distribution matching the spectrum. As this mode was used extensively in testing, the details of how the emulator was configured will now be described.

## Generating a Spectrum

A Python script was written to integrate over each of the individual waveforms (see Fig.10 and Fig.11) in an experimental data file. This integration performed by this script was simple and crude. The script would assign a column with a width matching the time resolution of the data and a height of the corresponding recorded voltage to each data point. The sum of all the columns in each waveform would then be dumped into a histogram to produce a spectrum similar to that of ADC spectrum. The integration could be improved by assigning a suitable trapezium to each data point or by using one of many other methods, however as only a representation of the equivalent ADC spectrum was needed to test the emulator, this was not implemented. See Fig.12 for an example histogram produced using this method, this holds, as expected, a similar shape characteristics as ADC spectra previously produced by the research group (where a fit was achieved using a convolution of a mirrored Landau, a Gaussian and then a Landau tail). If the spectrum was generated as described, from oscilloscope data, the bin width needs to be recorded so that the spectrum can be scaled accordingly via the emulator software interface.

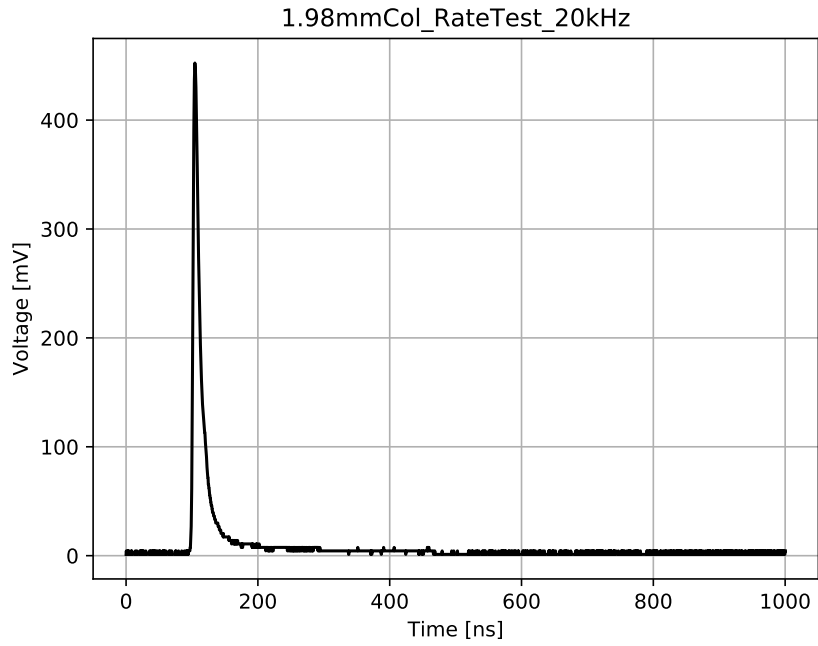


**Figure 10:** An single example waveform from the “1.98mmCol.7.24mmAbs.25kHzRate” data set collected at the Clatterbridge Cancer Centre, 02/08/2016. This was recorded using a Teledyne LeCroy HDO6104 oscilloscope. This has a time resolution of 0.4 ns and a voltage resolution of 0.2 mV

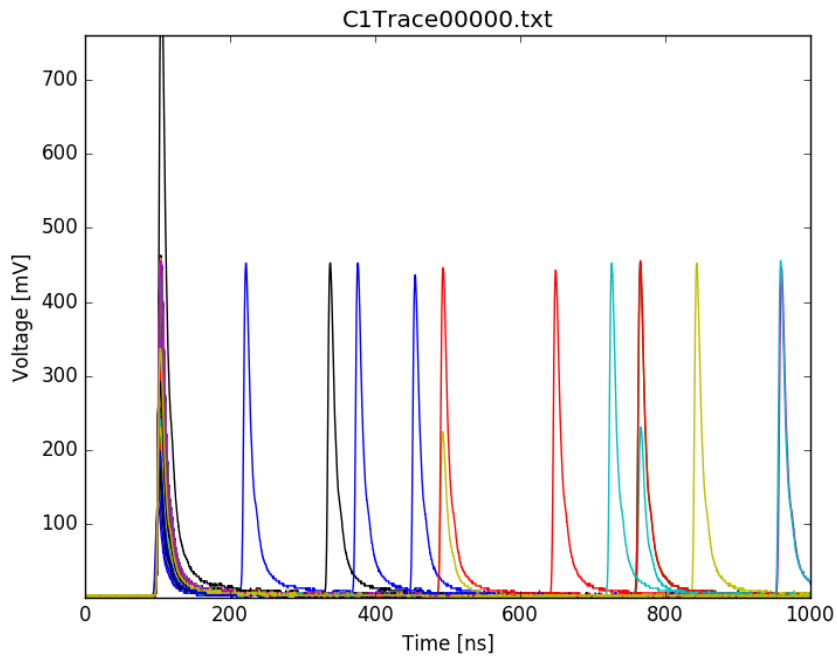


**Figure 11:** Overlay of 1000 waveforms in a single data file from the “1.98mmCol.7.24mmAbs.25kHzRate” data set collected at the Clatterbridge Cancer Centre, 02/08/2016. Note additional pulses beyond the trigger offset at 100 ns. Each colour trace represents an individual recorded waveform.



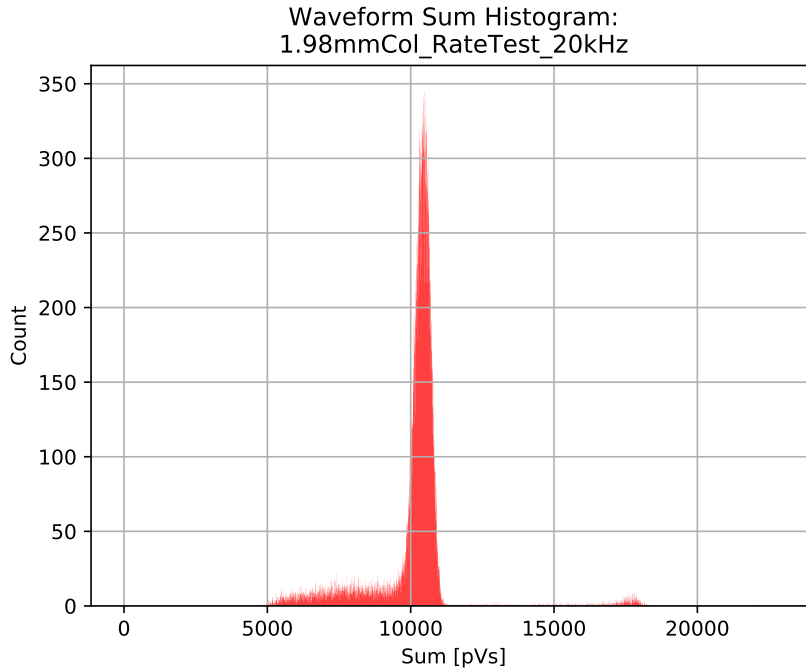


**Figure 12:** Histogram of the normalised sum (multiplied by step size) of individual waveforms using the data from the “1.98mmCol.7.24mmAbs.25kHzRate” run at the Clatterbridge Cancer Centre, 02/08/2016. This histogram uses 2502 line length waveforms, similar histograms were generated using different lengths to identify correct length. Modified versions of the Python program used to produce this histogram can generate spectrum files for use with the CAEN DT5800 detector emulator. Note the secondary peak at  $\sim 18000$  pVs. The units of pVs have been used for the bin values, if the data was generated from a digitiser this would be unit-less and would represent ADC channel.

### Spectrum Modifications

Ideally the method used to create the spectrum should be able to detect bad waveforms, such as those where pile-up has occurred, and discard them so that an “ideal” spectrum is generated. This is so that these features can be replicated more realistically using the emulator rather than just leaving the artefacts in the spectrum. For example, if the secondary peak from pile-up is in the spectrum, the emulator will take this as part of the “main” spectrum and simply generate pulses with double the area to recreate this secondary peak. To remove some of the bad pulses, a rather primitive method was used to remove that formed part of the spectrum beyond the Gaussian peak and Landau tail. This in effect removed the majority of the additional peaks from pile-up or that were abnormally large.

In order for the position of the spectra to be correct, in terms of ADC channel, the file containing the spectral shape needs to start from 0, i.e. if the first populated bin is at 5000 pVs then all prior unpopulated bins from 0 pVs to 5000 pVs need to be included in the spectrum file. Furthermore, it was observed that the x-axis of the spectrum should be scaled using the software interface when importing so that the spectrum is wide enough so that the finer details of the spectrum are reproduced. The simplest two ways to ensure the correct scale along this axis are to either scale by

the histogram bin width or to chose a bin width of 1 pVs when producing the spectral histogram. It was found to be best practice not to scale the spectrum along the y-axis (adjusting the peak), as this will exacerbate the features of the spectrum rendering the emulation inaccurate. An example of the adjusted and modified spectrum for the spectrum in Fig.12 can be seen in Fig.13.

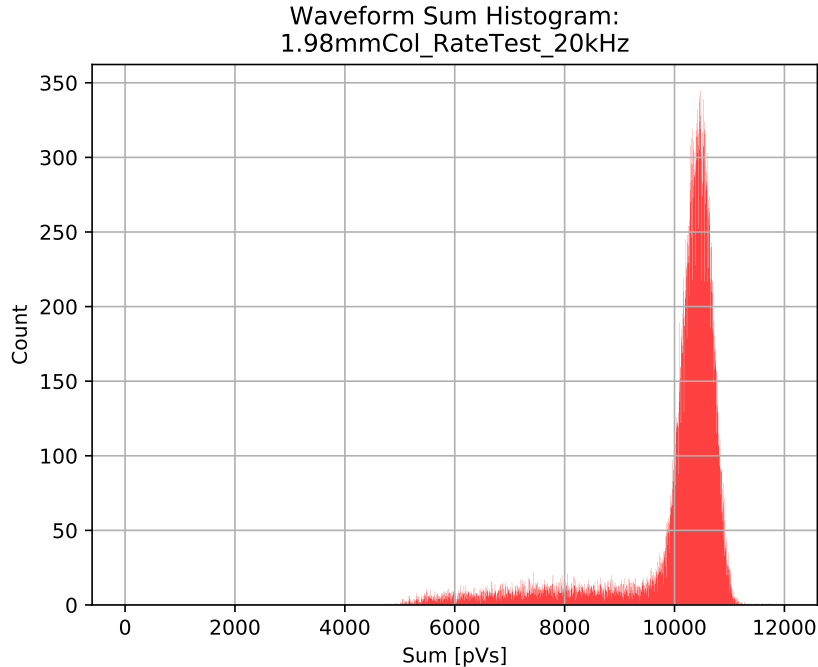


**Figure 13:** Modified spectral histogram containing data from the “1.98mmCol\_7.24mmAbs.25kHzRate” run at the Clatterbridge Cancer Centre, 02/08/2016. this is the final form of a histogram to be imported into the DT5800D detector emulator software interface. In comparison to Fig.12, note to absence of a secondary peak and that the bins start at 0 pVs. The units are added for clarity that the values are generated from integrals of the constituent waveforms (their areas). The bin width has also been changed to aid with scaling of the spectrum suing the detector emulator software interface. This could however be left unit less as this is spectrum is a representation of an ADC spectrum.

#### 4.2.2 Signal Shape Emulation

The detector emulator allows the user to customise the shape of the output signal pulse. The user can choose to either use the default exponential decay pulse, to define their own custom shape from a list of predefined modifiable inbuilt shapes or shape from an imported .csv file. In addition there is also the ability to generate a multi-shape pulse consisting of two defined signal shapes. In the evaluation of the detector emulator all of the inbuilt signal shapes were tested, these are suitable for simple emulations or in driving additional hardware such as an LED. As one of the aims of the evaluation was to emulate experiential data, an “ideal” waveform was produced from experimental for use with the detector emulator.

#### Generating an “Ideal” Waveform

Although a signal from a PMT can be roughly characterised using a single or exponential equation (see eq.(9)), finding the parameters from fitting a function to characterise a typical signal from a

specific data set would not be straight forward due to the energy/area distribution as seen in Fig.12. Therefore, the chosen method to generate an ideal waveform/signal was to take a selection of “good” waveforms and produce an average signal from them.

In order to do this, what characterised a “good” waveform needed to be defined. Thousands of unique waveforms were recorded per data set, including bad waveforms that would otherwise be rejected, which required the definition to ignore many waveforms. By using the already produced histogram of signal areas, this definition could be relatively simply defined by inspection of the distribution. By inspecting the primary Gaussian shaped peak in the spectrum a short range of waveform areas around the peak could be identified. This, all be it a rather vague and qualitative method, did filter out the majority of bad waveforms, selected only the most common waveforms and selected enough waveforms so that a satisfactory average could be produced. This process was all completed via Python script. The averaging function simply generated a single waveform where each point in this waveform was the average of each of the corresponding points in the selected “good” waveforms.

### **Resolving Resolution Issues**

This averaging created a waveform that had the same time resolution as the original data recorded by the oscilloscope which was found to be far finer than what the detector emulator was able to reproduce. Since the shape file does not have a column representing the time values of each data point, it was necessary to create a new shape file that has the data points from the average waveform mapped onto its coarser time resolution. The resolution/time-step for imported signal shapes is not directly stated in the detector emulator user manual. This was simply calculated by dividing the maximum length a signal shape could be by the maximum number of points that the signal shape can be defined by and found to be 6.348 ns. See Fig.14 for a comparison between a “good” average waveform with the resolution of the oscilloscope and a waveform with the data points mapped to the resolution of the detector emulator.

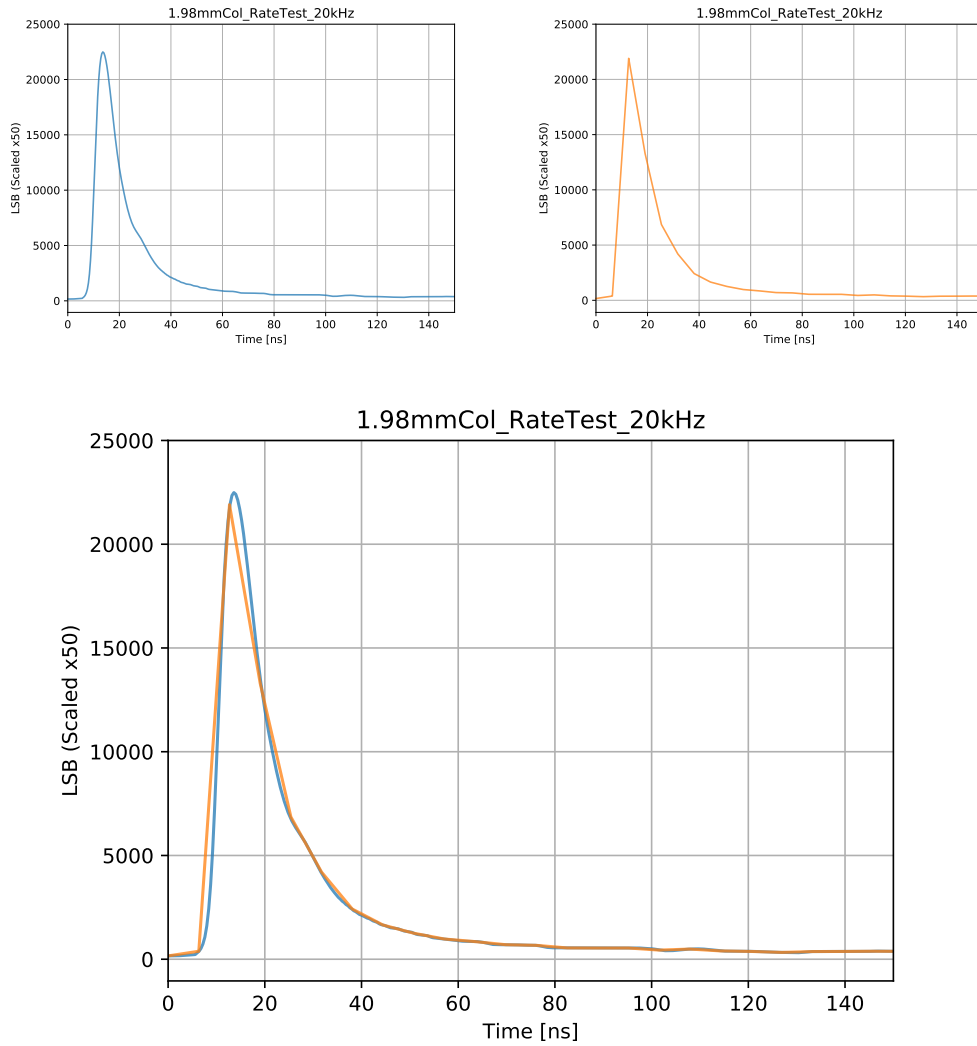


**Figure 14:** Comparison between a “good” average waveform with the native resolution (from oscilloscope) and the same waveform after being mapped onto data points with the time resolution for the detector emulator. Both waveforms in this figure have been converted to LSB, scaled and trimmed. Data from the “1.98mm-Col.7.24mmAbs.25kHzRate” run at the Clatterbridge Cancer Centre, 02/08/2016. From top left clockwise: oscilloscope resolution waveform (blue trace), detector emulator resolution waveform (orange trace), overlay of both waveforms. Lines between data points have been included for signal shape clarity.

## Changing Units

When importing a custom signal shape into the detector emulator, the signal cannot be defined in terms of volts. Instead it needs to be defined in terms of least significant bit (LSB). In [46] the conversion is stated as eq.(10), where the 4 V value refers to the voltage range of output signals (-2 V to 2 V). However, this conversion was not suitable as the imported spectrum did not have a matching range. Therefore a more general equation was used to find the scale for converting from volts to LSB (see eq.(11)) where  $V_{\text{ref}}$  is taken as the voltage of most populated bin (this is easiest identified using the detector emulator GUI).

$$\text{LSB} = \frac{4 \text{ V}}{2^{16}} \quad (10)$$

$$\text{LSB} = \frac{V_{\text{ref}}}{2^{\text{bits}}} = \frac{V_{\text{ref}}}{2^{16}} \quad (11)$$

### Further Modifications

The imported signal shape was further modified by removing data points (trimming) associated with the dead-time surrounding signal recorded by the oscilloscope (i.e. before trigger and after the pulse). These values which were near to 0 mV (not exactly 0 mV due to dark current) needed to be removed so that they were not counted as part of the emulated signal. If left in, this would inhibit the ability to follow the energy spectrum and implement some artificial noise (in particular pile-up). The dark current also had to be subtracted from each of the data points as otherwise, after scaling during emulation, the tail of the signal would form a plateau not tending to 0 mV. The baseline of the average signal was also adjusted so that it was  $\sim 0$  mV and no longer the opposite polarity of the signal pulse.

### Final Scaling

Unfortunately due to how the detector emulator interpolates between data points when generating a signal, there is an averaging effect between points where  $\frac{dV}{dt}$  is large and when  $\frac{dV}{dt}$  changes polarity quickly. i.e. The emulator struggles to reproduce fine details in an imported shape. This was very significant for the emulation of experimental data as by re-representing the waveform at the lower resolution for the correct length signal to be generated, the short pulse is only defined by a few data points. This then meant that the output signal was significantly smaller than required. Therefore the values in the data file needed to be scaled larger. It is difficult to formally and quantitatively describe by how much an imported signal needs to be scaled by as this depends on how detailed the signal is and its magnitude. The orange trace in Fig.14 shows the final form of a waveform that has had all the necessary steps performed so that it is ready to be emulated.

#### 4.2.3 Time Distribution

The time distribution of signals generated by the detector emulator can be defined by one or four separate methods; at a constant rate, with a Poisson distribution, a custom user defined distribution or custom user defined sequence of events. Since the sample sequence mode on the oscilloscope was used to record experimental data, the exact rate and time distribution of the experimental data could not be determined. Therefore, for the testing/evaluation of the custom distribution and sequence time distribution modes, arbitrary distributions and sequences were used to verify how these modes worked.

A more in depth evaluation of the constant rate and Poisson time distribution methods was undertaken. These both worked as expected, however it should be noted that the constant rate is

defined in terms of kilo counts per second (kcps) where this is equivalent to kHz (i.e.  $1 \text{ kcps} \equiv 1 \text{ kHz}$ ).

#### 4.2.4 Emulator Output

For each iteration of testing the various features of the detector emulator, the signal was output to the Teledyne LeCroy HDO6104 oscilloscope. By using the inbuilt oscilloscope mathematics and graphing functions, it was possible to quickly inspect the output by eye to evaluate if the detector emulator was behaving as expected. The most commonly used inbuilt function/multi-function was to produce an on-the-fly histogram of the signal area. An example of this function in practice can be seen in Fig.15 where this shows an “acceptable” emulation of the experimental data from the “1.98mmCol\_RateTest\_20kHz” run at the Clatterbridge Cancer Centre, 02/08/2016 with all of the above described manipulations applied to the spectrum and signal shape. A comparison between the histogram output from the oscilloscope with the corresponding raw binned experimental data (not adjusted for time-step) can be seen in Fig.16 where both histograms have the same bins. Both histograms have the same shape implying the emulation is accurate however it can be seen that the histogram for the experimental data is shifted to the left, this is expected as the integration does not account for the negative baseline voltage and the integration gates are wider. As mentioned earlier, the negative baseline has been taken into account for the emulation, albeit in a relatively crude manner, when generating the average “good” waveform shape.

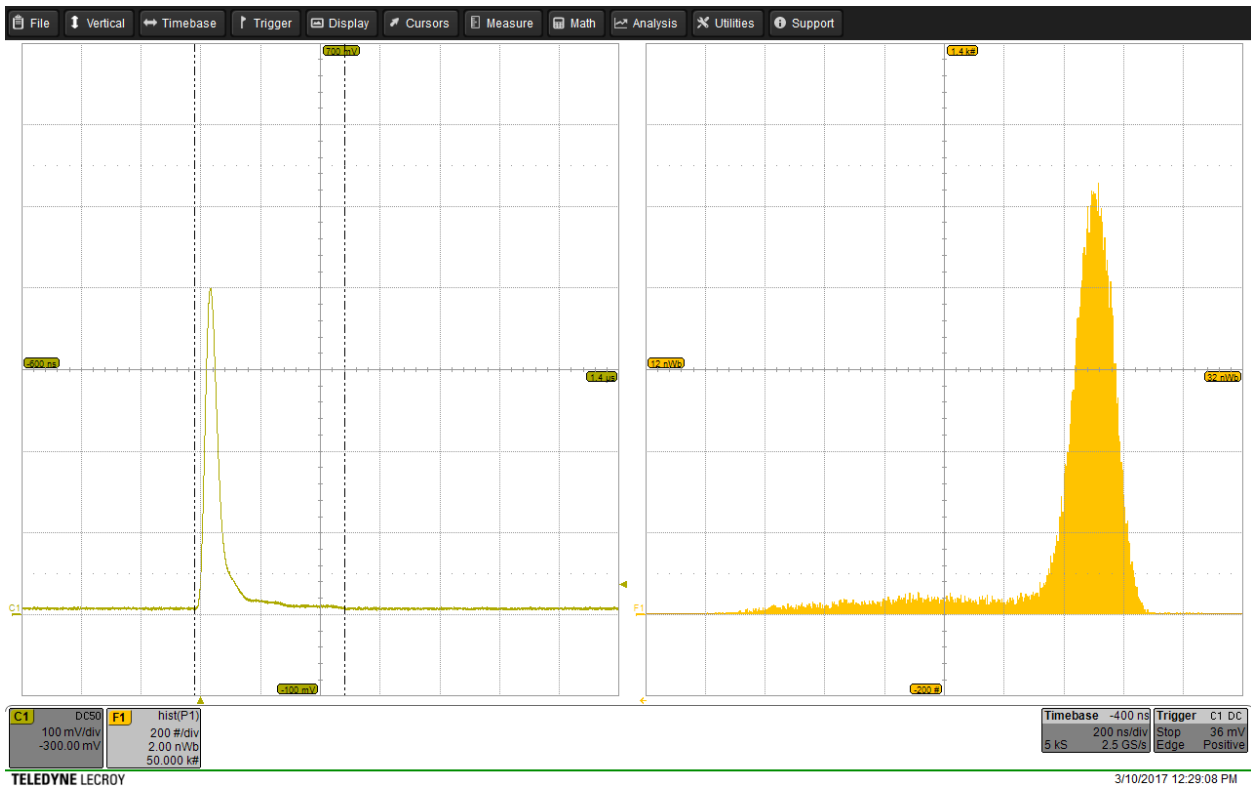


**Figure 15:** Output from detector emulator from an acceptable emulation as seen on an oscilloscope. Left hand side show an example signal with the vertical integration gates and the start end end of the pulse. Right hand image shows a histogram of the areas of the triggering signals between these gates. Note the similarity of the shape pulse when compared to the low resolution pulse in Fig.14 and the shape of the histogram compared to the spectral histogram in Fig.13.

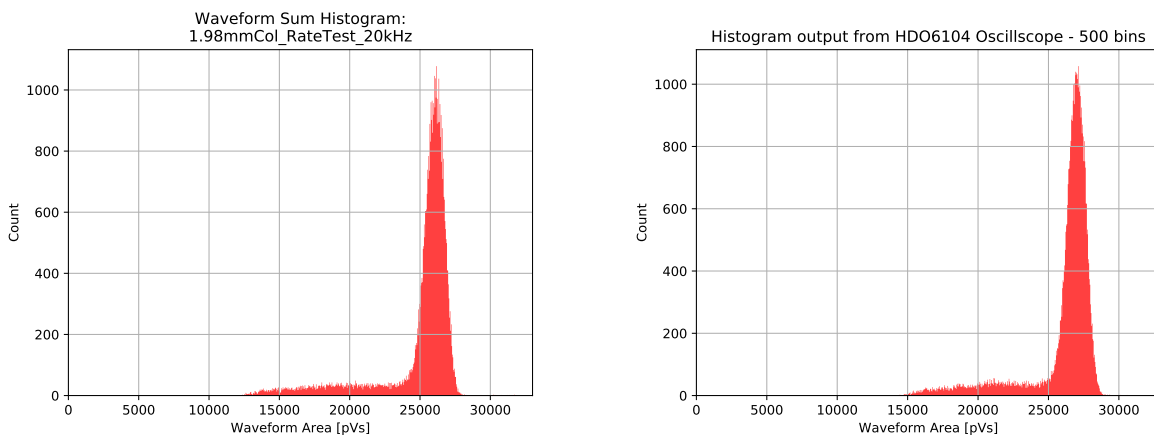


**Figure 16:** Left hand plot: histogram for the the raw experimental data from the “1.98mm-Col.7.24mmAbs\_25kHzRate” run at the Clatterbridge Cancer Centre, 02/08/2016. This histogram have not been adjusted for the time-step of 0.4 ns, as in Fig.12 and Fig.13. Nor did the method of integrating the waveforms take into account the negative baseline. Right hand plot: the histogram in Fig.15 replotted. In both plots, the histogram bins have the same position, size and widths.

#### 4.2.5 Noise and Interference Emulation

Artificial noise and interference can applied to an emulation, this is programmable within the detector emulator software interface. These programmable features are: random number noise, white noise,  $1/f$  noise, baseline drift, random walk, shot noise, interference and pile-up. All types

of noise emulation, besides baseline drift and interference, can only be programmed by adjusting one/two variables. Baseline drift can be set by either using the GUI to draw how the baseline changes or by importing a .csv file contain this pattern. Interference is set by importing a .csv file with the interference pattern then choosing the time distribution and magnitude of the interference.

Each of the artificial noise features was individually tested. The feature whose effect can most easily be implemented to replicate experimental data is pile-up. Typically the second (or greater) peak(s) originate from two (or more) pulses falling within the same time window (pile-up). The additional peaks can be re-created by increasing the maximum number of events in pile-up to the number of desired peaks, enabling parallelisation so that multiple pulses can overlap, and reducing the dead-time to 0 ns. An example of this feature being implemented, with the same signal shape and spectrum as is Fig.15, can be seen in Fig.17. Unfortunately the user cannot adjust the probability of pile-up occurring, hence making it difficult to change to parameters so that the ratio between the main and additional peaks are correctly replicated as in Fig.12. It should also be noted that if the constant rate time distribution is used, pile-up cannot be emulated.

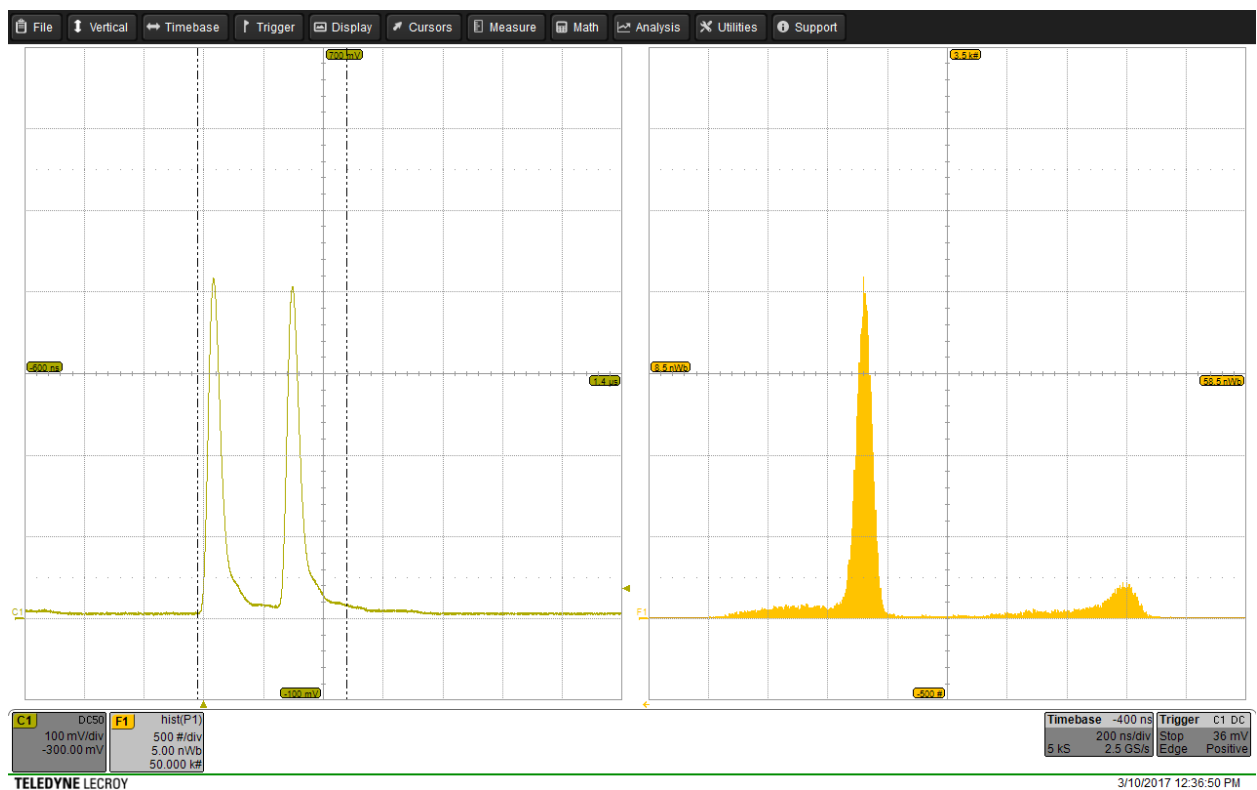


**Figure 17:** Image of oscilloscope output for the same emulation parameters as in Fig.15 with addition emulated pile-up. Left hand image: an example pile-up event within the integration gates. Right hand image: a signal area histogram for between the integration gates.

One could extend the length of the imported signal shape to the length of the oscilloscope recording window minus the trigger offset. This would allow more realistic pile-up to be emulated similar to that in Fig.11.



Although a PMT has an associated statistical noise known as shot noise, the shot noise feature in the detector emulator will not produce the same effect and should not be used to emulate this. The artificial shot noise feature of the detector emulator randomly generates Gaussian-like pulses of a user defined magnitude with a user defined probability of occurring. This is not the same thing as PMT shot noise. Instead, the better choice of programmable noise to emulate PMT shot noise would be random number or white noise. These would be more suitable because they are more constant and average (closer) to zero. Whereas emulated shot noise is always the same polarity as the signal (see Fig.18). It may be useful to try and emulate PMT shot/statistical noise because the random fluctuations in the signals is lost in the creation of an average waveform. For this to be effective, the magnitude of the programmed random number or shot noise should be very small relative to the signal amplitude.

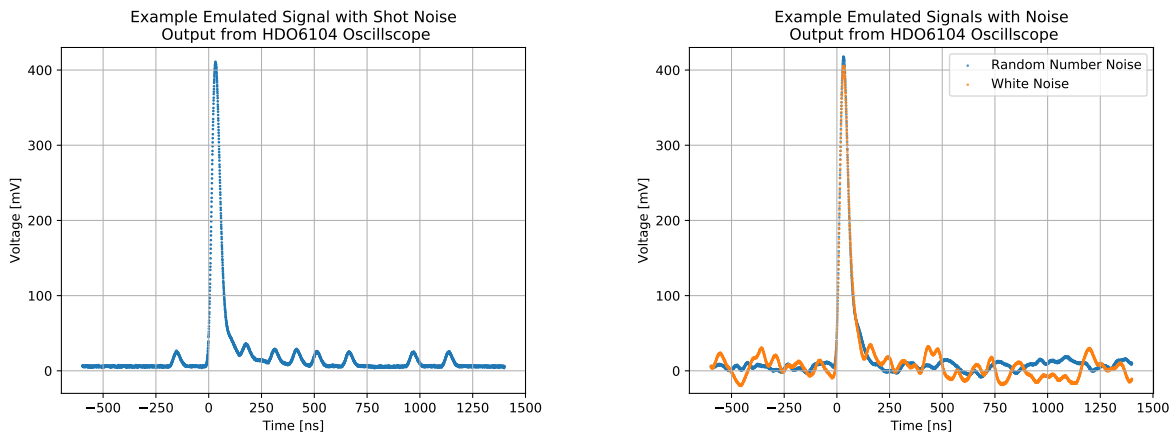


**Figure 18:** Left hand plot: an example emulated signal with added shot noise. Right hand plot: comparison between example emulated signals with added random number or shot noise. Both emulations with added random number and white noise have the same programmed magnitude (800 LSB, 0.0258 V). This magnitude is far larger than what should be used, it has been exaggerated here to show the noise contribution.

### 4.3 Limitations

The main limitation of the DT5800D detector emulator for emulating experimental data of this kind is its ability to generate short and finely detailed pulses. As mentioned before, this is from the relatively coarse resolution of  $\Delta t = 6.348$  ns between data points for imported signal shapes. This limitation results in a very qualitative trial and error method having to be implemented when scaling the signal shape and a final output signal where the constituent data points can easily be identified.

Another set of limitations, that are more of an inconvenience, are how the some of the features are programmed within the detector emulator software interface. For example not being able to directly specify a probability for pile-up occurring, not being able to change the units in the spectrum display plot from LSB to V but being able to change samples to  $\mu s$ , and that some

features sporadically need to be selected then deselected and re-selected in order to be implemented.

#### 4.4 Evaluation of Potential Uses

Overall the detector emulator is capable of emulating experimental data that is comparable to the original data. Therefore verifying its suitability for being used to test different methods of data collection and on-the-fly data processing without either having the detector running or using a radiation source. The convenience of being able to do this in a laboratory environment is a particular advantage due to the nature of the application of proton therapy beamlines and their relative scarcity. Every experimental run completed during business hours uses time that could be used to treat patients which, from a hospital's point of view, is a higher priority.

The accuracy of the emulation is, as mentioned before, limited by the time-step resolution and the qualitative scaling of the signal shape to compensate for the consequences of the resolution. The quality of future emulations could be improved by using a more robust method for identifying and discarding bad waveforms from the ADC (or ADC equivalent) spectrum and a better method for integrating over individual waveforms.

Due to the aforementioned limitations, a better application of the detector emulator may be to use it to drive an LED that injects light into the detector's PMT. Hence, providing another method of stress-testing the detector. This application does not depend on the time-step resolution. The detector emulator has been tested and proven to be able to generate the simple pulses that have been previously used to drive an LED in PMT testing. However the stability of the generated signals have not been investigated. Using the detector emulator in role complicates the implementation of programmable noise potential rendering all noise features, bar pile-up, non-applicable.

In the future, if used in conjunction with an improved spectrum, it would be beneficial to investigate how the other programmable noise features could be implemented. This should not be too time intensive as there are not many variables the user can change.

## 5 PMT Testing

### 5.1 Rationale

As described in Section 2.3 the prototype detector uses one of two identical PMTs with different electronics bases. Previous investigations had shown that the PMT gain response differed between the two as the rate of incident photons on the photocathode increases. This frequency dependence of the PMT gain required further investigation because, in its intended application, the detector could be subject to a wide range of incident particle rates. Variations in the response of the Hamamatsu

base PMT was also noticed in detector tests using the proton beamline at the Clatterbridge Cancer Centre when using different beam rates. The different response for the Hamamatsu based PMT therefore was most likely to be a result of the included active divider circuit.

## 5.2 Experimental Set Up

To test the the detector under under laboratory conditions, a pulser driven,  $\sim 400$  nm LED was used to inject light into the polystyrene scintillator via an optical fibre. The photons from this light injection would then scatter inside the scintillator and fall incident on the PMT's photocathode inducing photoelectron emission instigating the amplification within the PMT generating a signal. A  $\sim 400$  nm LED was used because of the manufacture stated spectral response of the PMT has a range of 300 nm to 650 nm with the peak wavelength for maximum cathode radiant sensitivity being stated as 420 nm.

The output signal from the PMT was either output directly to a CAEN DT5751 digitiser, directly to a Teledyne Lecroy HDO6104 oscilloscope, or the signal was passed through a discriminator and inverter in a NIM crate before being input to the CAEN DT5751 digitiser. The reason for the use of the NIM electronics was to try to reduce background and to invert the signal (see Fig.19 for a schematic of the experimental set up). The digitiser could either use an external signal to indicate when it should be triggered or use an inbuilt self/software trigger. When using the external trigger, the trigger signal from the pulser was sent directly to the digitiser. The CAEN DT5751 digitiser has the capability to not only record input signals but is also able to integrate and bin signal into histogram generating an ADC spectrum on-the-fly.

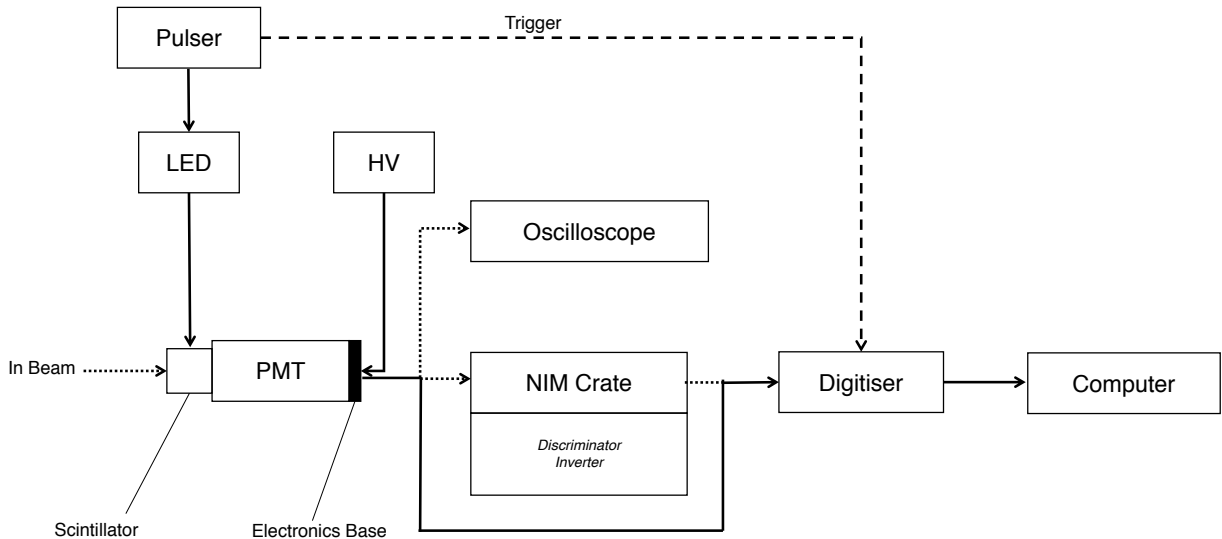


**Figure 19:** Basic schematic of the experimental set up for pulsed light injection. HV is the high voltage supply to the PMT.

### 5.3 Method

The HV power supply was set to 900V for every LED rate test, this is a typical supply voltage for the used PMT. For each rate test the pulser was configured to produce a 20 ns positive square signal with a 5 ns rise and fall time. The amplitude of the pulser signal to drive the LED was set to  $\sim 2.14$  V, this voltage was chosen because it would generate a PMT output signal of a similar magnitude to what would be produced from experimental runs using the Clatterbrige beamline.

Before recording data, it was necessary to wait a period of time, around 2 hours, after initially turning the pulser on so that the LED could stabilise. During the stabilisation period, the pulse would usually be left at 100 Hz. A similar approach was taken every time the pulser frequency was changed, where it was also necessary to wait a short period of time, 1 - 5 minutes, for the LED to re-stabilise at the new operating frequency.

Next the digitiser was configured for the desired triggering method. If using the software trigger, this including adjusting the threshold to a level where the majority of the background tail in the histogram did not contribute to the signal part of the histogram. An example of an ADC spectrum using the software trigger with a threshold of 0 LSB can be seen in Fig.20, the background is everything to the left of the right hand Gaussian peak. The threshold level used for the majority of tests using the software trigger was 90 LSB, this is quite high but this got rid of almost all of the tail and did not noticeably effect the non-background part of the ADC spectrum.

Other digitiser settings were also set. Some important settings to note included the length of short gate, length of the long gate and the charge sensitivity. These were 150 ns, 151 ns and 20 fC/LSB respectively and were kept the same for all tests. The dual integration gates could be set to different lengths and configured to try and identify bad waveforms, but since these tests were completed by injecting light from a relatively stable LED the number of bad waveforms should be negligible.

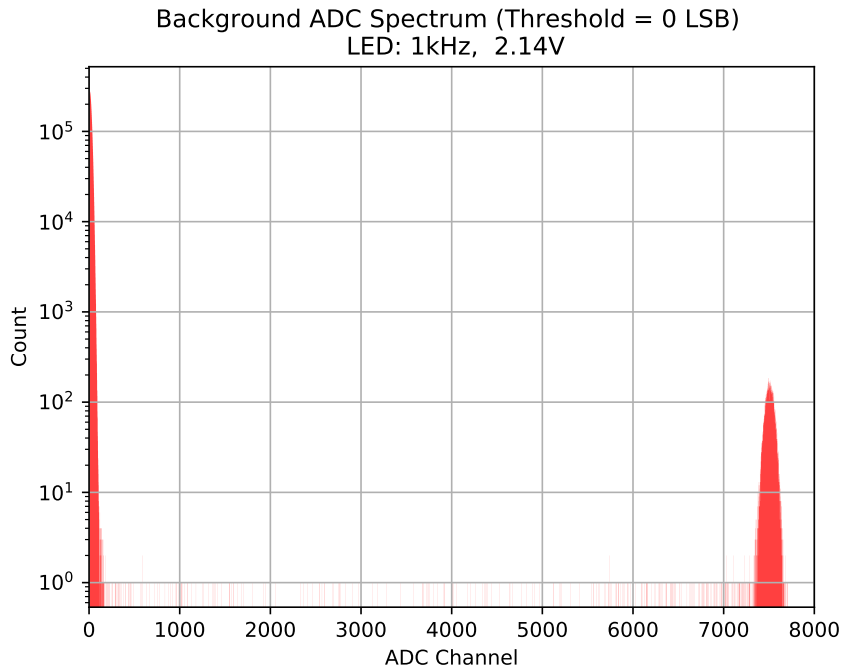


**Figure 20:** An example ADC spectrum for the Hamamatsu base PMT using the CAEN DT5751 digitiser software trigger with 0 LSB threshold so that background can be seen.

After the configuration and the initial stabilisation period the pulser frequency was set, left for a couple of minutes to re-stabilise, the histogram was cleared and the digitiser was left for a short period of time so that a sufficient sample size of waveforms were integrated and binned into the histogram. Once the energy histogram data was saved the pulser frequency would be increased and the process repeated.

As seen in the right hand peak of Fig.20 with a large number of samples the distribution of waveform energies appears and was assumed to be Gaussian. Therefore for each histogram produced using this experimental method, a Gaussian distribution eq.(12) was fitted so that the mean ADC channel,  $\mu$ , and standard distribution,  $\sigma$ , could be extracted. For the fitting, a Python script was written that utilised the SciPy curve\_fit function [47]. The free parameters for the fit were  $\mu$ ,  $\sigma$  and a scalar  $c$  (see. eq.(13)). For initial guesses of these free parameters  $\sigma$  and  $c$  were always 200 and 400 respectively. These values were chosen by inspection. For the initial guess for  $\mu$ , the Python script would search for and find the most populated bin/ADC channel. The uncertainty in the

mean,  $\Delta\mu$ , could be calculated using the standard error (see eq.(14)). However since the sample sizes were very large,  $\Delta\mu \ll \mu$ . An example fit can be seen in Fig.21. This method was used with both PMT bases with both triggering methods over short (100 Hz - 5 kHz) and long (1 kHz - 500 kHz) pulser frequency ranges.

$$\mathbf{G}(x, \mu, \sigma) = \frac{1}{\sigma\sqrt{2\pi}} e^{-\frac{(x-\mu)^2}{2\sigma^2}} \quad (12)$$

$$\mathbf{F}(x, \mu, \sigma, c) = c \mathbf{G}(x, \mu, \sigma) \quad (13)$$

$$\Delta\mu = \pm \frac{\sigma}{\sqrt{N_{\text{samples}}}} \quad (14)$$

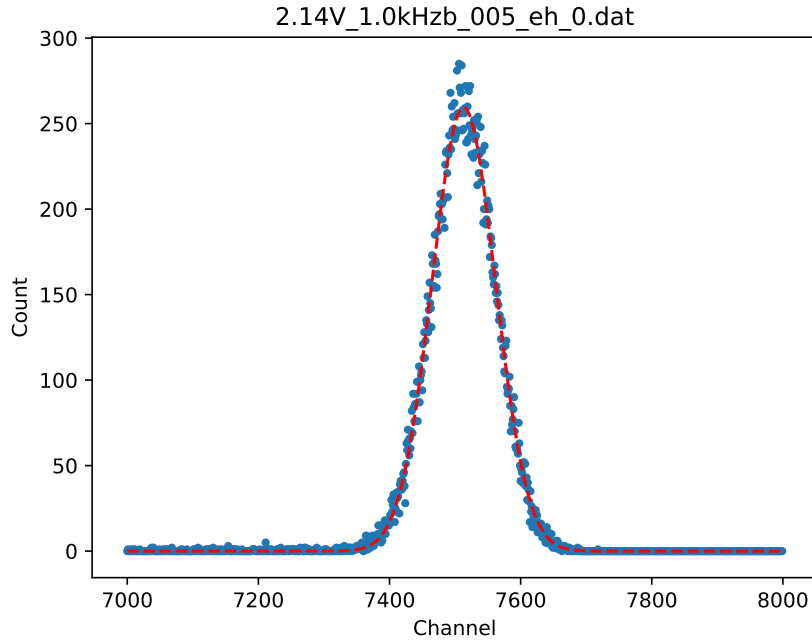


**Figure 21:** A example ADC spectrum histogram with eq.(13) fitted to the data points. The ADC spectrum has been cropped so that the fit over the Gaussian portion of the histogram can be seen. This plot is a showing data from the Hamamatsu base PMT with a supply voltage of 900 V, with the pulser set at 1 kHz with an amplitude of 2.14 kHz and the collected using the DT5751 digitiser in self/software trigger mode. The title of the figure refers to the CAEN .dat data file where the “b” after the stated frequency refers to this being a background run with the threshold set to 0 LSB.

## 5.4 Results

### 5.4.1 Wide Frequency Range

Using the above describe method a data point,  $(\mu, f)$ , with an associated uncertainty could be generated for each pulser frequency. The results of which, for a wide range of pulser frequencies (1 kHz - 500 kHz) for both the Hamamatsu and UCL base PMTs can be seen in the first row of

Fig.22. These two plots show the relationship between how the peak of the normally distributed histogram of waveform integrals changes as frequencies change.

It can be seen that both PMTs have a similar response at frequencies below 50 kHz. However, as the frequency of the pulser was increase beyond this the Hamamatsu base PMT’s response stayed relatively stable in comparison to the UCL base PMT where the mean ADC channel increased dramatically with frequency. The data point at 100 kHz for the Hamamatsu base PMT was an anomalous result that could not be replicated.

The standard deviation of each Gaussian fit and the mean can be seen in the second row of Fig.22 where it appears that the standard deviation increases as the mean ADC channel increases for both PMTs. This is likely to be a property of the LED rather than the PMTs.

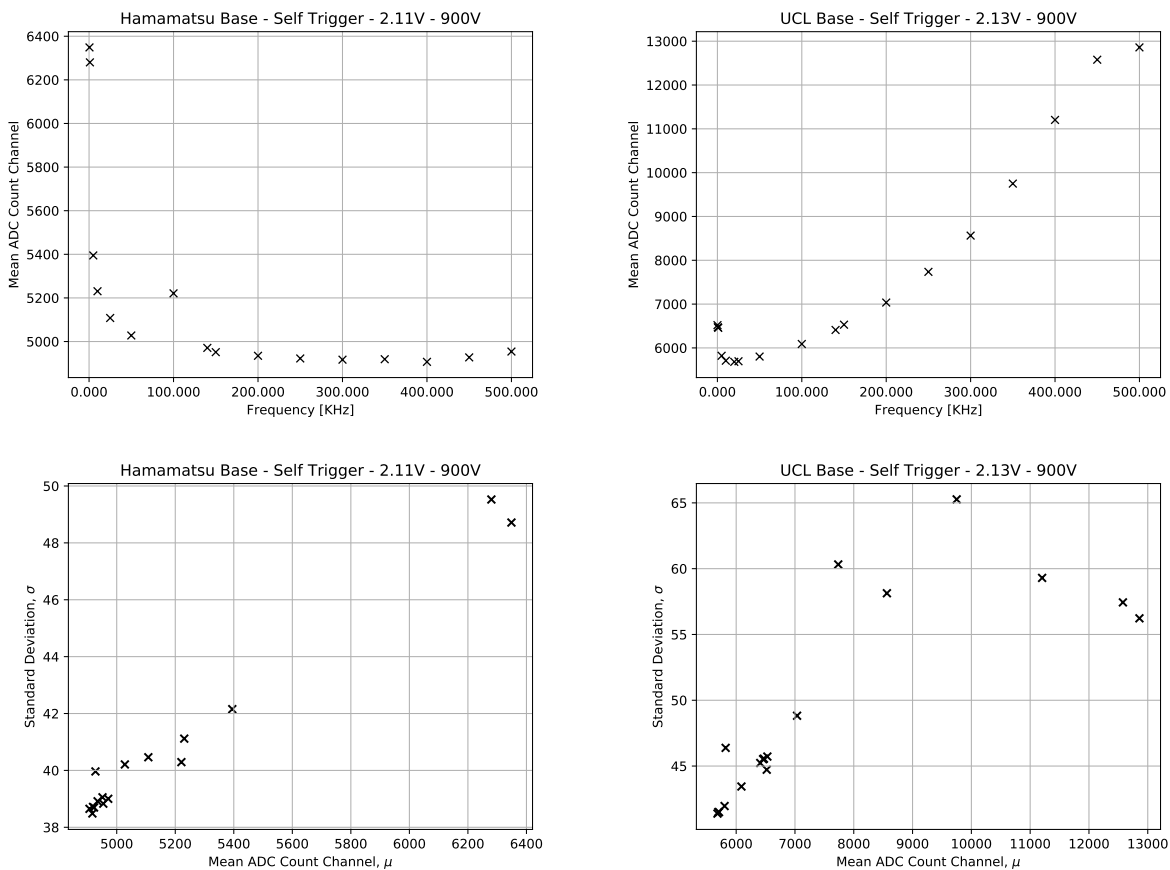


**Figure 22:** Comparison between Hamamatsu and UCL base PMTs over a wide range of injected light pulse frequencies. Left hand column: LED light injected in to the Hamamatsu base PMT. Right hand column: LED light injected into UCL base PMT. Top row: mean ADC count channel at different frequencies of LED light pulses. Bottom row: standard deviation from Gaussian fit vs mean ADC count channel. All data collected using CAEN DT5751 digitiser in self/software trigger mode. It should be noted that the plots in this figure are not “zeroed”.

Since the sample size was large and the ADC spectrum could be modelled as Gaussian, it was possible to be able to estimate the number of photoelectrons,  $N_{p.e.}$ , at the anode using eq.(15) [48]. From this and the digitiser charge sensitivity/resolution ( $DCS = 20 \text{ fC/LSB}$ ) the gain of the PMT,

$g$ , could be estimated at each frequency using eq.(16). The results of using these two relationships with the above data can be seen in Fig.23.

$$N_{p.e.} \approx \left(\frac{\mu}{\sigma}\right)^2 \quad (15)$$

$$g \approx \mu \frac{DCS}{N_{p.e.}e} \quad (16)$$

Across the full range of frequencies, the estimated number of photoelectrons for the Hamamatsu base PMT was fairly stable and did not fluctuate by more than 1%. The gain however was considerably greater at lower frequencies. For the UCL base PMT, the estimated number of photoelectrons remained fairly uniform up until the high frequencies where the number increased significantly. The gain plots for both PMTs has similar shapes as with the mean channel plots, but from the UCL base PMT the gain appears to drop with pulser frequencies of 400 kHz and greater.

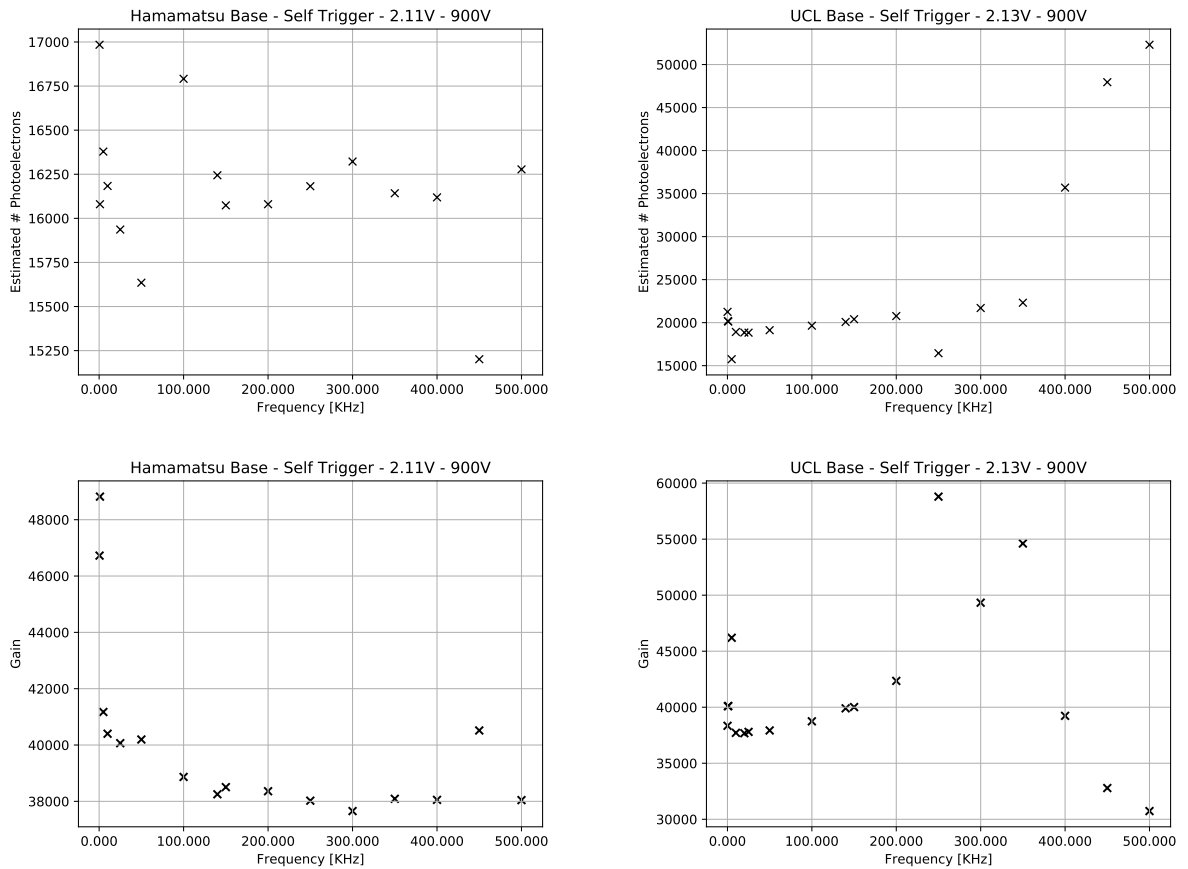


**Figure 23:** Comparison between Hamamatsu and UCL base PMTs over a wide range of injected light pulse frequencies. Left hand column: LED light injected in to the Hamamatsu base PMT. Right hand column: LED light injected into UCL base PMT. Top row: estimated number of photoelectrons collected at the PMT anode at different frequencies of LED light pulses. Bottom row: estimated gain vs frequency. All data collected using CAEN DT5751 digitiser in self/software trigger mode. It should be noted that the plots in this figure are not “zeroed”.



Although the peak voltage supplied by the pulser to the LED was different for the data collected for the two different PMTs, the difference was small enough so that the general trends could still be compared. Frequency dependence should be and was shown to still be apparent at both voltages. This meant that the exact values could not be compared, although this would still not be possible even if the voltage was exactly the same because the optical properties for the transfer of light between the fibre and scintillator, and the scintillator and PMT change every time the detector is disassemble/reassembled. This is because the volume of BC-630 used to couple the components and the coupling itself was not precisely controlled.

#### **5.4.2 Narrow Frequency Range**

Since the greatest change in gain for the Hamamatsu base PMT occurred at lower frequencies, the method was repeated at lower frequencies with smaller pulser frequency step sizes. This was done using both the software/self trigger of the digitiser and using the external trigger. Data was recorded with pulser frequencies ranging from 100 Hz to 5 kHz, with 100 Hz increments. The results of these repeats can be seen in Fig.24.

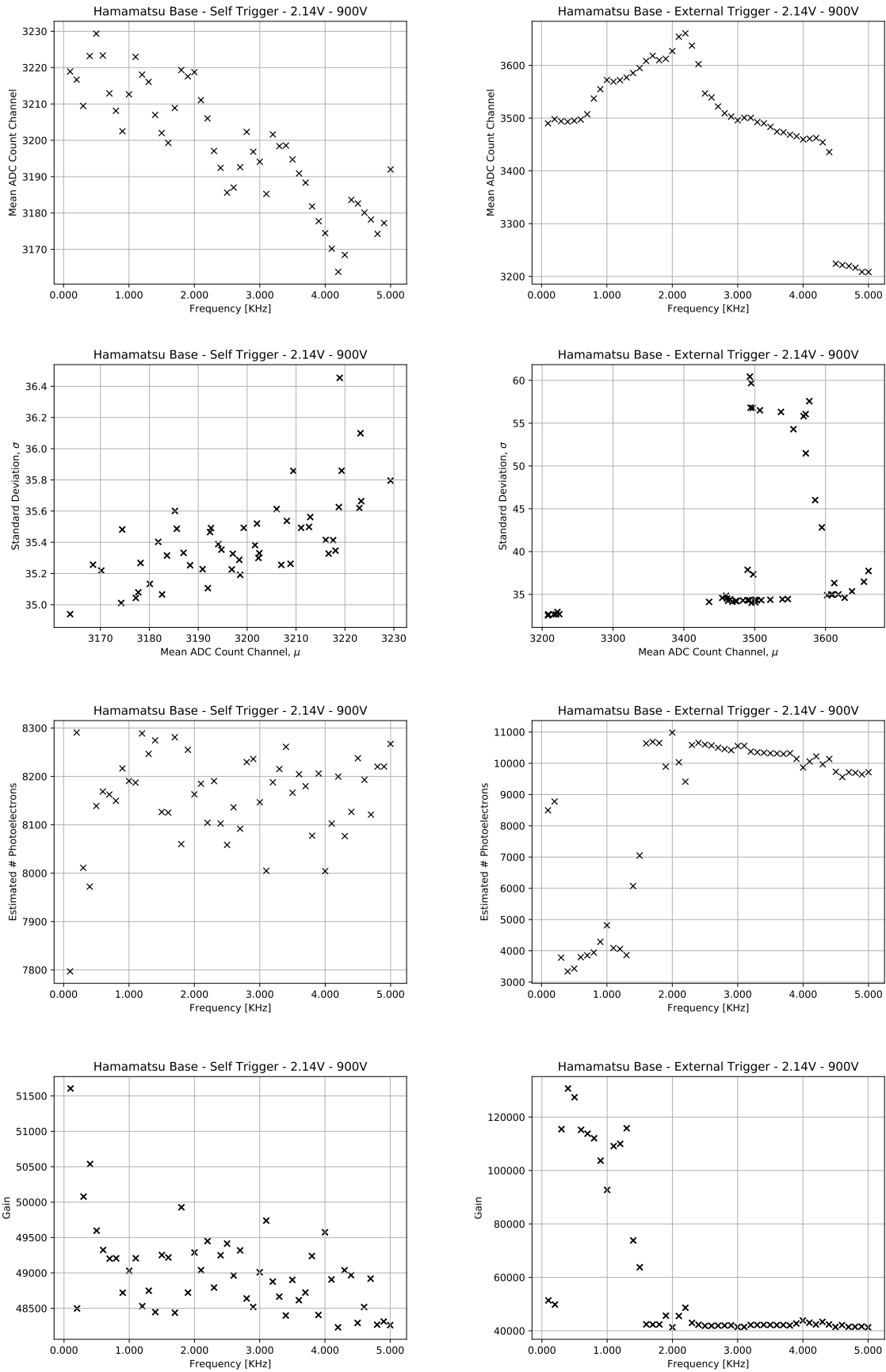


**Figure 24:** Hamamatsu base PMT response over a short range of injected light pulse frequencies. Figure also compares results from self/software and external digitiser trigger modes. Left hand column: self/software trigger mode. Right hand column: external trigger mode. First row: mean ADC count channel vs frequency. Second row: standard deviation from Gaussian fit vs mean ADC count channel. Third row: estimated number of photoelectrons collected at the PMT anode vs frequency. Bottom row: estimated gain vs frequency. All data collected using CAEN DT5751 digitiser in self/software trigger mode. It should be noted that the plots in this figure are not “zeroed”.

With both triggering modes the variation in mean ADC count channel is less than 1% across all frequencies. Apart from at the highest 6 frequencies when using the external trigger mode, a shift occurred in the ADC spectrum occurred at 4.5 kHz and all subsequent record spectra were also shifted. This shift was a common occurrence when recording data and often happened randomly. Shifts would also occur if the detector was disturbed.

The estimated number of photoelectrons and gain did not vary by more than 1% either over the whole range of pulse frequencies when using the self/software trigger mode. By contrast, when using the external trigger these two estimates varied considerably with increasing pulser frequency, particularly at lower frequencies. Why there would be a such a difference in frequency response (not values) between the two triggering methods is unknown.

### 5.4.3 Fixed Peak Current

The method was modified so that the peak anode current,  $I_{\text{peak}}^{\text{anode}}$ , was set to 10 mA. This was achieved by outputting the PMT signal to an oscilloscope and adjusting peak pulser signal voltage until the desired peak current was matched. The current could be calculated as the resistance,  $R$ , was known to be  $50 \Omega$  and using an averaged signal on the oscilloscope. The time width at the full width half maximum of the signal,  $\Delta t_{\text{FWHM}} = 11 \text{ ns}$ , was also noted so that the gain,  $g$ , could be calculated using eq.17. The measured parameters were  $V_{\text{Pulser}} = 2.22 \text{ V}$  and  $\Delta t_{\text{FWHM}} = 11 \text{ ns}$ . The same method of increasing the pulser frequency was then continued ranging from 500 Hz to 1 MHz. The relationship between the full width half maximum, FWHM, and standard deviation for a Gaussian distribution can be seen in eq.(18).

$$g = \frac{I_{\text{peak}}^{\text{anode}} \Delta t_{\text{FWHM}}}{N_{\text{p.e.}} e} = \frac{V_{\text{peak}} \Delta t_{\text{FWHM}}}{R N_{\text{p.e.}} e} \quad (17)$$

$$\text{FWHM} = 2\sqrt{2 \log(2)} \sigma \approx 2.35\sigma \quad (18)$$

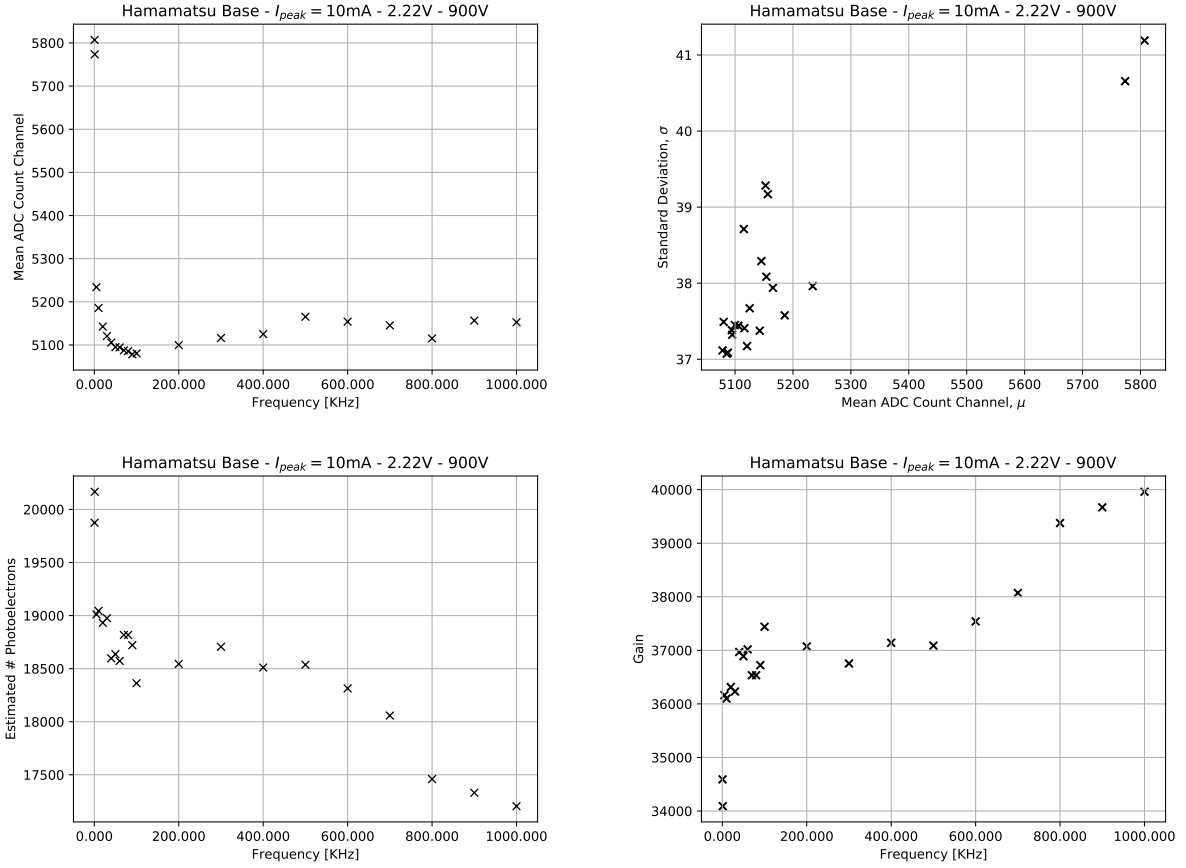


**Figure 25:** Plots from data collected using the Hamamatsu base PMT after adjusting pulser signal voltage so that  $I_{peak}^{anode} = 10\text{ mA}$ . From left to right clockwise: mean ADC count channel vs pulser frequency, standard deviation from Gaussian fit vs mean ADC count channel, estimated number of photoelectrons vs pulser frequency, gain vs pulser frequency. It should be noted that the plots in this figure are not “zeroed”.

The overall general trend for the mean ADC count channel with increasing pulser frequency (top left plot Fig.25) was, as expected, similar to that in previous tests of the Hamamatsu base PMT without setting the peak current (top left plot Fig.22). A small, but apparent dependency for the gain at different frequencies can be seen on the bottom right plot in Fig.25.

#### 5.4.4 Anomalous Results

While taking data to investigate the PMT responses many anomalous responses were observed and recorded. The source of some could be identified, such as shifts in the ADC spectrum peak when the detector was disturbed. Whereas other could not be traced, such as other sporadic shifts in the ADC spectrum peak when the detector had remained untouched.

Shifts in the ADC spectrum peak when the detector was disturbed was mostly due to the the coupling between the scintillator and PMT changing under sudden movement. Due to the non-permanent optical coupling, measures were taken to not move the detector or any attached cabling or components whilst data was being collected. However sometimes this could not be avoided.

Many shifts did occur without any disturbance to the detector, but did tend to occur after the the pulser had been running for a prolonged period of time.

It was also observed that often waiting 2 hours for the LED to initially stabilise was not long enough. this was noticed when some measurements performed at the same frequency directly after the initial stabilisation period were repeated later and the ADC spectrum peak was noticeably different.

A repeat of the measurements conducted to collect the data shown in Fig.25 but using the UCL base PMT was attempted. When this was attempted, it was observed that the signal from the PMT was fluctuating rapidly between two values, resulting in a double peak in the ADC spectrum. This was of course not a typical response for the PMT and was attributed to either recent modifications to the base where additional pins were soldered to the last dynode and ground, or damaged caused in recent transportation of the PMT. This anomalous response of the PMT at different supply voltages, using identical pulser signals (shape, peak voltage and frequency), can be seen in a combined ADC spectrum in Fig.26. It was interesting to note that the anomaly became more apparent at the more typical supply voltages. This anomaly had no real significance besides from indicating that the PMT base needed to fixed/modified.

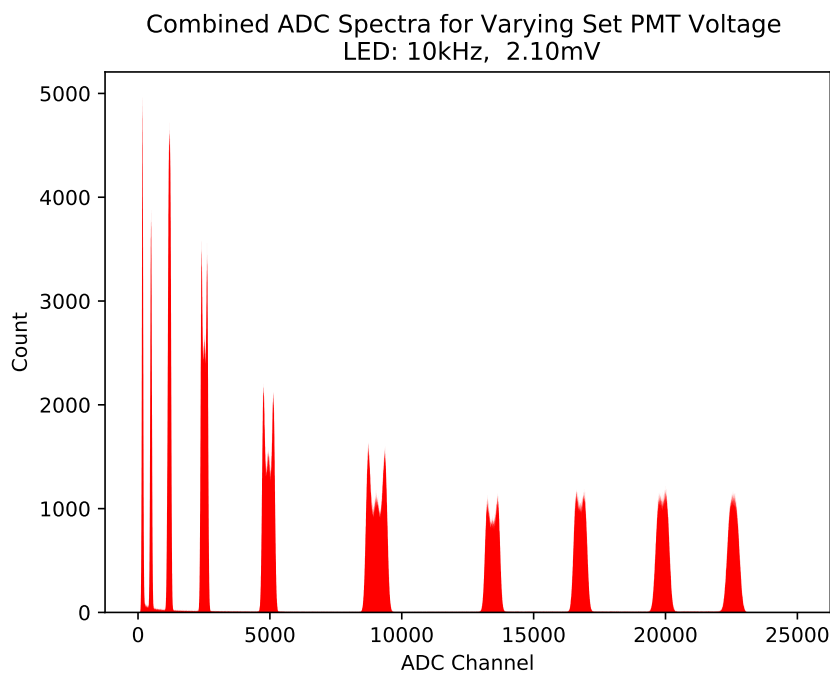


**Figure 26:** Combined ADC spectrum for anomalous results from UCL base PMT at different PMT supply voltages. From left to right the peaks are for supply voltages from 500 V to 1400 V in 100 V steps. Only the position and shape of each peak should be considered when looking at this plot.

## 6 Conclusion

In conclusion, the CAEN DT5800D detector emulator can effectively emulate experimental data, however many time consuming qualitative methods have to be applied when constructing the required waveform shape and energy spectrum in order to overcome the emulator's shortfalls. The most significant shortfall that effects the research group's intended application of the emulator is the time step between each data point used to form the signal shape. The time step is too wide to accurately reproduce a signal whose FWHM is less than  $\sim 15$  ns, unless the data points are scaled larger. The accuracy to the energy spectrum produced by an emulation could be improved by using better methods of discarding bad waveforms and integrating good waveforms when generating a spectrum to be imported into the detector emulator. Information about the discarded bad waveforms could then be used to improve the configuration of programmed noise in the emulation. Overall, the emulations produced by the detector emulator would be suitable for testing hardware and analysis software in the absence for a detector or detector and radiation source.

A Teledyne LeCroy oscilloscope was also successfully characterised for high frequency data acquisition. This included configuring the oscilloscope so that there was minimal data loss from non continuous acquisition and producing a conversion script to convert this recorded data to a format compatible with legacy analysis tools.

With regards to PMT testing, it was observed that the addition of an active divider circuit does change the response of a PMT with different frequencies of injected light. The most apparent difference was the gain at frequencies greater than  $\sim 100$  kHz, where the gain for the PMT with the active divider circuit remained fairly constant whereas the gain of PMT without the active divider circuit changes considerably. The most important gain frequency dependence that should be noted was at low pulser frequencies whereby the PMT with the active divider circuit did exhibit a very slight dependence. The results from this investigation that formed part of this report only provide a general overview of the gain-frequency dependence of the PMTs with and without the active divider circuit. Therefore, to further quantify and validate this relationship and the other PMT responses, a more controlled and intricate investigation is required.

## References

- [1] A. Coates, *et al.*, “On the Receiving End Patient Perception of the Side-Effects of Cancer Chemotherapy”, *Eur. J. Cancer*, vol. 19, no. 2, pp. 203-208, 1983.
- [2] R. Wilson, “Radiological Use of Fast Protons”, *Radiology*, vol. 47, no. 5, pp. 487-491, 1946.
- [3] J. Slater *et al.*, “Development of a Hospital-Based Proton Beam Treatment Center”, *Int. J. Radiat. Oncol., Biol., Phys.*, vol. 14, no. 4, pp. 761-775, 1988.
- [4] D. Bonnett *et al.*, “The 62 MeV Proton Beam for the Treatment of Ocular Melanoma at Clatterbridge”, *Br. J. Radiol.*, vol. 66, no. 790, pp. 907-914, 1993.
- [5] C. Patrignani *et al.*, “Review of Particle Physics”, *Chin. Phys. C*, vol. 40, no. 10, p. 100001, 2016.
- [6] A. Smith, “Proton Therapy”, *Phys. Med. Bio.*, vol. 51, no. 13, pp. R491-R504, 2006.
- [7] A. Koehler *et al.*, “Range Modulators for Proton and Heavy Ions”, *Nucl. Instr. Meth.*, vol. 131, no. 3, pp. 437-440, 1975.
- [8] W. Levin *et al.*, “Proton Beam Therapy”, *Br. J. Cancer, BJC*, vol. 93, no. 8, pp. 849-854, 2005.
- [9] H. Palmans *et al.*, “Water Calorimetry and Ionization Chamber Dosimetry in an 85-MeV Clinical Proton Beam”, *Med. Phys.*, vol. 23, no. 5, pp. 643-650, 1996.
- [10] S. Vatnitsky, “Radiochromic Film Dosimetry for Clinical Proton Beams”, *Appl. Radiat. Isot.*, vol. 48, no. 5, pp. 643-651, 1997.
- [11] L. Zhao and I. Das, “Gafchromic EBT Film Dosimetry in Proton Beams”, *Phys. Med. Bio.*, vol. 55, no. 10, pp. N291-N301, 2010.
- [12] G. Cirrone *et al.*, “A 62-MeV Proton Beam for the Treatment of Ocular Melanoma at Laboratori Nazionali del Sud-INFN”, *IEEE Trans. Nucl. Sci.*, vol. 51, no. 3, pp. 860-865, 2004.
- [13] “Zebra with OmniPro-Incline Brochure”, IBA Dosimetry, 2016. [Online]. Available: [http://www.iba-dosimetry.com/sites/default/files/RT-BR-E-Zebra-OP-Incline-0211\\_Rev.2\\_0813.pdf](http://www.iba-dosimetry.com/sites/default/files/RT-BR-E-Zebra-OP-Incline-0211_Rev.2_0813.pdf). [Accessed: 13- Oct- 2016].
- [14] R. Grant *et al.*, “Relative Stopping Power Measurements to Aid in the Design of Anthropomorphic Phantoms for Proton Radiotherapy”, *J. Appl. Clin. Med. Phys.*, vol. 15, no. 2, pp. 121-126, 2014.
- [15] S. Dhanesar *et al.*, “Quality Assurance of Proton Beams Using a Multilayer Ionization Chamber System”, *Med. Phys.*, vol. 40, no. 9, p. 092102, 2013.
- [16] B. Arjomandy *et al.*, “An Overview of the Comprehensive Proton Therapy Machine Quality Assurance Procedures Implemented at The University of Texas M. D. Anderson Cancer Center Proton Therapy Center-Houston”, *Med. Phys.*, vol. 36, no. 6, pp. 2269-2282, 2009.
- [17] L. Verhey *et al.*, “The Determination of Absorbed Dose in a Proton Beam for Purposes of Charged-Particle Radiation Therapy”, *Radiat. Res.*, vol. 79, no. 1, pp. 34-54, 1979.
- [18] E. Grusell *et al.*, “Faraday Cup Dosimetry in a Proton Therapy Beam Without Collimation”, *Phys. Med. Bio.*, vol. 40, no. 11, pp. 1831-1840, 1995.
- [19] C. Gomà *et al.*, “Proton Beam Monitor Chamber Calibration”, *Phys. Med. Bio.*, vol. 59, no. 17, pp. 4961-4971, 2014.

- [20] S. Lin, T. *et al.*, “More Than 10 Years Experience of Beam Monitoring with the Gantry 1 Spot Scanning Proton Therapy Facility at PSI”, *Med. Phys.*, vol. 36, no. 11, pp. 5331-5340, 2009.
- [21] A. Beddar, “Water Equivalent Plastic Scintillation Detectors in Radiation Therapy”, *Radiat. Prot. Dosim.*, vol. 120, no. 1-4, pp. 1-6, 2006.
- [22] M. Bucciantonio *et al.*, “Development of a Fast Proton Range Radiography System for Quality Assurance in Hadron Therapy”, *Nucl. Instr. Meth. Phys. Res., Sect. A*, vol. 732, pp. 564-567, 2013.
- [23] A. Freshville, “Calorimeter R&D for the SuperNEMO Double Beta Decay Experiment”, *JPCS*, vol. 293, p. 012037, 2011.
- [24] V. Bashkirov *et al.*, “Novel Scintillation Detector Design and Performance for Proton Radiography and Computed Tomography”, *Med. Phys.*, vol. 43, no. 2, pp. 664-674, 2016.
- [25] J. Argyriades *et al.*, “Spectral Modeling of Scintillator for the NEMO-3 and SuperNEMO Detectors”, *Nucl. Instr. Meth. Phys. Res., Sect. A*, vol. 625, no. 1, pp. 20-28, 2011.
- [26] G. Knoll, *Radiation Detection and Measurement*, 4th ed. Hoboken, N.J.: John Wiley & Sons, 2010.
- [27] M. Clift *et al.*, “Dealing with Cerenkov Radiation Generated in Organic Scintillator Dosimeters by Bremsstrahlung Beams”, *Phys. Med. Bio.*, vol. 45, no. 5, pp. 1165-1182, 2000.
- [28] J. Birks, “Scintillations from Organic Crystals: Specific Fluorescence and Relative Response to Different Radiations”, *Proc. Phys. Soc. A*, vol. 64, no. 10, pp. 874-877, 1951.
- [29] G. O’Rielly, *et al.*, “The Response of Plastic Scintillator to Protons and Deuterons”, *Nucl. Instr. Meth. Phys. Res., Sect. A*, vol. 368, no. 3, pp. 745-749, 1996.
- [30] R. Winyard, *et al.*, “Pulse Shape Discrimination in Inorganic and Organic Scintillators. I”, *Nucl. Instr. Meth.*, vol. 95, no. 1, pp. 141-153, 1971.
- [31] L. Bollinger and G. Thomas, “Measurement of the Time Dependence of Scintillation Intensity by a Delayed-Coincidence Method”, *Rev. Sci. Instr.*, vol. 32, no. 9, pp. 1044-1050, 1961.
- [32] C. Zorn, “A Pedestrian’s Guide to Radiation Damage in Plastic Scintillators”, *Radiat. Phys. Chem.*, vol. 41, no. 1-2, pp. 37-43, 1993.
- [33] A. Bross and A. Pla-Dalmau, “Radiation Damage of Plastic Scintillators”, *IEEE Trans. Nucl. Sci.*, vol. 39, no. 5, pp. 1199-1204, 1992.
- [34] K. Jang, *et al.*, “Fiber-optic Cerenkov Radiation Sensor for Proton Therapy Dosimetry”, *Opt. Express*, vol. 20, no. 13, p. 13907, 2012.
- [35] L. Austin and H. Starke, “Ueber die Reflexion der Kathodenstrahlen und eine damit verbundene neue Erscheinung Secundärer Emission”, *Ann. Phys.*, vol. 314, no. 10, pp. 271-292, 1902.
- [36] B. Lubsandorzhev, “On the History of Photomultiplier Tube Invention”, *Nucl. Instr. Meth. Phys. Res., Sect. A*, vol. 567, no. 1, pp. 236-238, 2006.
- [37] *Photomultiplier Tubes, Basics and Applications, Third Edition (Edition 3a)*, Hamamatsu Photonics K.K., 2007. [Online]. Available: [https://www.hamamatsu.com/resources/pdf/etd/PMT\\_handbook\\_v3aE.pdf](https://www.hamamatsu.com/resources/pdf/etd/PMT_handbook_v3aE.pdf). [Accessed: 14 Oct- 2016].



- [38] W. Leo, *Techniques for Nuclear and Particle Physics Experiments*, 2nd ed. Berlin, Heidelberg: Springer Berlin Heidelberg, 1994.
- [39] D. Green, *The Physics of Particle Detectors*, 1st ed. Cambridge, U.K.: Cambridge University Press, 2000.
- [40] J. Wilson and J. Hawkes, *Optoelectronics: An Introduction*, 3rd ed. Harlow, England: Prentice Hall, 1998.
- [41] *Photomultiplier Tubes, Photomultiplier Tubes and Related Products*, Hamamatsu Photonics K.K., 2016. [Online]. Available: [http://www.hamamatsu.com/resources/pdf/etd/PMT\\_TPMZ0002E.pdf](http://www.hamamatsu.com/resources/pdf/etd/PMT_TPMZ0002E.pdf). [Accessed: 19-Mar- 2017].
- [42] *PHOTOMULTIPLIER TUBES R13478, R13449, R13408, R13089*, Hamamatsu Photonics K.K., 2016. [Online]. Available: [https://www.hamamatsu.com/resources/pdf/etd/R13478\\_R13449\\_R13408\\_R13089\\_TPMH1363E.pdf](https://www.hamamatsu.com/resources/pdf/etd/R13478_R13449_R13408_R13089_TPMH1363E.pdf). [Accessed: 27- Mar- 2017].
- [43] “Operator’s Manual, HDO6000, High Definition Oscilloscopes, 922499 Rev B, November 2013”, Teledyne LeCroy, Inc., 2013. [Online]. Available: [http://cdn.teledynelecroy.com/files/manuals/hdo6000\\_om-a.pdf](http://cdn.teledynelecroy.com/files/manuals/hdo6000_om-a.pdf). [Accessed: 8- Jan- 2017].
- [44] “LeCroy X-Stream Oscilloscopes, Remote Control Manual, February 2005, WM-RCM-E Rev D”, LeCroy Corporation, 2005. [Online]. Available: [http://cdn.teledynelecroy.com/files/manuals/wm-rcm-e.rev\\_d.pdf](http://cdn.teledynelecroy.com/files/manuals/wm-rcm-e.rev_d.pdf). [Accessed: 8- Jan- 2017].
- [45] “lecroy.py, Commit Date: 07/05/2016, License: MIT”, 2016. [Online]. Available: <https://github.com/freespace/pylecroy/blob/master/lecroy.py>. [Accessed: 8- Jan- 2017].
- [46] “User Manual UM3074, Digital Detector Emulator, Emulation of Digital Pulses from Radiation Detectors, Rev. 3 - 29 January 2016”, CAEN S.p.A., 2016. [Online]. Available: <http://www.caen.it/servlet/checkCaenManualFile?Id=11354>. [Accessed: 8- Jan- 2017].
- [47] E. Jones, *et al.*, “SciPy: Open Source Scientific Tools for Python”, 2001-. [Online]. Available: <http://www.scipy.org/>. [Accessed: 24- Mar- 2017].
- [48] A. Basharina-Freshville, “Search for the neutrinoless double beta decay of  $^{100}\text{Mo}$  with the NEMO3 detector and calorimeter research and development for the SuperNEMO experiment”, Ph.D. Thesis, Dept. Phys. & Astron. , University College London, London, United Kingdom, 2011.